Report on

Plans of the Beams Division

for

TeV33

April 16, 1997

J. Marriner, editor

Contributors:

C. Ankenbrandt
P. Bagley
F. Bieniosek
M. Church
J. Johnstone
I. Kourbanis
D. McGinnis
J. Marriner
S. Ngaitsev
S. O'Day
R. Pasquinelli
S. Shukla
S. Werkema

1. Colliding beam parameters & Overview

The Tevatron antiproton collider achieved a peak luminosity of 2.5×10^{31} $cm^{-2}sec^{-1}$ in Run I, which ended in February 1996. The Main Injector, the Recycler Ring, and the associated colliding beams upgrades are expected to enable luminosities in the range of 8×10^{31}–2×10^{32} $cm^{-2}sec^{-1}$ in Run II, which is scheduled to begin late in 1999. These upgrades are sometimes collectively referred to as Fermilab III. The addition of the Recycler Ring to the Main Injector project is expected to improve the antiproton utilization efficiency and accounts for a factor of 2 to 3 of the luminosity increase..

The goal of the TeV33 project is to increase the peak luminosity to the vicinity of 10^{33} $cm^{-2}sec^{-1}$. A more specific goal of obtaining 30 fb^{-1} by the year 2006 was suggested in the TeV2000 committee report.[1] The TeV33 period of collider running is also referred to as Run III.

Table I is the working parameter table for Run II. It illustrates the changes required to achieve the Run II luminosity goals and also the benefits of antiproton recycling. Run II requires a modest improvement in proton intensity and about 8 times more antiprotons (spread over 6 times more bunches). The antiproton stacking rate is required to increase substantially (about a factor of 3) to produce the necessary antiprotons. The Run II luminosity also benefits from the smaller (2 eV-sec) longitudinal emittances expected from the Main Injector, the higher energy (1000 GeV instead of 900 GeV) Tevatron, and the higher antiproton transmission efficiency of the Main Injector.

Table I. Working parameter table for Run II.

Parameter	Run IB (1993-95)*	Run II (w/Recycler)	Units
Protons/bunch	23×10^{10}	27×10^{10}	
Antiprotons/bunch	5.5×10^{10}	7.5×10^{10}	
Req'd Pbar Production Rate	6	20	10^{10}/hr
Proton emittance (95%, norm)	23π	20π	mm-mrad
Antiproton emittance (95%, norm)	13π	15π	mm-mrad
Energy	900	1000	GeV
No. of Bunches	6	36	
Bunch length (rms)	0.60	0.38	m
Form Factor	0.59	0.73	
Typical Luminosity	1.6×10^{31}	2.1×10^{32}	$cm^{-2}sec^{-1}$
Bunch Spacing	~3500	396	nsec
Interactions per crossing	2.7	5.8	

*Run IB column represents average of 32 stores over the period March 8-April 21, 1995.

1.1 Collider Luminosity

The luminosity of the Tevatron collider may be written as

$$L = \frac{3\gamma_r f_0}{\beta^*}\left(BN_{\bar{p}}\right)\left(\frac{N_p}{\varepsilon_p}\right)\frac{F\left(\beta^*,\theta_x,\theta_y,\varepsilon_p,\varepsilon_{\bar{p}},\sigma_z\right)}{\left(1+\varepsilon_{\bar{p}}/\varepsilon_p\right)} \qquad [1]$$

where $\gamma_r=E/mc^2$ is the relativistic energy factor, f_0 is the revolution frequency, and β^* is the beta function at s=0 (where it is assumed to attain the same minimum in each plane). The proton (antiproton) beam transverse emittance $\varepsilon_p\,(\varepsilon_{\bar{p}})$ is defined to be $\varepsilon = 6\pi\gamma_r\sigma^2/\beta$ for a bunch with a gaussian distribution and assumed to be the same in both transverse planes, B is the number of bunches, $N_p\,(N_{\bar{p}})$ is the number of protons (antiprotons) per bunch, θ_y and θ_y are the crossing half-angles, σ_z is obtained from the rms proton and antiproton bunch lengths $\sigma_z^2 = \left(\sigma_{zp}^2 + \sigma_{z\bar{p}}^2\right)/2$ and $F\leq 1$ is a form-factor that accounts for the depth of focus (hourglass) and crossing angle effects on the luminosity caused by non-zero bunch lengths. The bunch lengths depend on the longitudinal emittance and the rf voltage, but the luminosity depends only on the bunch lengths. In Run II, the form-factor is dominated by the hourglass effect (the design crossing-angle is 0). For gaussian beams the hourglass effect may be written as:

$$F = \frac{\sqrt{\pi}\beta}{\sigma_z}\, e^{\frac{\beta^2}{\sigma_z^2}}\,\mathrm{erfc}\left[\frac{\beta}{\sigma_z}\right] \qquad [2]$$

where the complementary error function is related to the error function by $\mathrm{erfc}(z) = 1-\mathrm{erf}(z)$. For TeV33 the crossing angle effect is large and the luminosity comes mainly from the z=0 region where the hourglass effect is small. In this case the form-factor F may be written as

$$F = \frac{1}{\sqrt{1+\sigma_z^2\left(\theta_x^2/\sigma_x^2 + \theta_y^2/\sigma_y^2\right)}} \qquad [3]$$

where $\sigma_x^2 = \left(\sigma_{xp}^2 + \sigma_{x\bar{p}}^2\right)/2$ and similarly for y.

The luminosity formula ([1]) is written to emphasize the major issues in achieving high luminosity. The first quantity in parentheses is the total number of antiprotons. Under current and probably future operating conditions, the most important factor contributing to the achievable luminosity is the total number of antiprotons in the ring, $BN_{\bar{p}}$. The second most important factor is the proton phase space density, N_p/ε_p, which is constrained by the need to limit the beam-beam tune shift. The form-factor (F) and the emittance ratio factor $\varepsilon_p/\left(\varepsilon_p+\varepsilon_{\bar{p}}\right)$ are important, but they cannot exceed unity and the amount of luminosity that can be gained using these factors is limited.

1.2 Importance of Antiproton Production

Of the many technical issues involved with high luminosity proton-antiproton colliders, there is probably no more fundamental limitation than the requirement that antiprotons must be produced at least as rapidly as they are consumed in beam-beam collisions. The minimum production rate is

$$\Phi_{\bar{p}}^{(\min)} = n_c \sigma_a L \qquad [4]$$

where n_c is the number of collision points and L is the luminosity. The cross-section is the cross-section for scattering outside the acceptance of the Tevatron. This cross-section is only slightly less than the total cross-section. We assume that σ_a is 70 mb at 1000 GeV. With 2 collision points a luminosity of 10^{33} cm^{-2}-sec^{-1} is sustained with a minimum antiproton production rate of 50×10^{10} hr^{-1}.

A more realistic estimate of the antiproton flux must take into account the fact that antiprotons beam-beam collisions are not the only mechanism for antiproton loss. We define the antiproton utilization efficiency as the number of antiprotons lost through beam-beam collisions divided by the total number of antiprotons produced. During the latter part of Run Ib the antiproton utilization efficiency was about 7%.*

The second consideration in determining the antiproton flux required is that neither the luminosity nor the stacking rate is constant. For example, during the Run Ib period referred to above the Tevatron was producing beam-beam collisions for the experiments 51% of the time. The average initial luminosity of these stores was 1.25×10^{31} cm^{-2}-sec^{-1}, but the average rate of accumulating luminosity during a store (29 nb^{-1}/hr) corresponds to a luminosity 64% lower. Thus, the Run Ib experience is consistent with the "Snowmass Criterion": that the integrated luminosity obtained is equal to the peak luminosity times the length of the run divided by 3. The peak stacking rate during Run Ib was $7.2x10^{10}$ hr-1. During the same Run Ib running period the antiproton source was stacking 62% of the time at an average rate of $4.3x10^{10}$ hr-1 (60% of the peak value). Thus, the total number of antiprotons accumulated was 37% (also roughly 1/3) of the peak rate times the length of the run. It should be noted that the percentages of time given for both the Tevatron and the Antiproton Source have no corrections for effects such as scheduled and unscheduled maintenance; they represent actual operating experience during an extended run.

The antiproton utilization efficiency must increase dramatically for Run II when the luminosity is expected to increase to 2×10^{32} $cm^{-2}sec^{-1}$ from the Run Ib value of 2×10^{31} $cm^{-2}sec^{-1}$ while the stacking rate increases from 7×10^{10} hr^{-1} to 20×10^{10} hr^{-1}. If the duty factors and efficiencies experienced in Run Ib were to remain the same, then the antiproton utilization efficiency would have to increase to 42%. However, the use of the Recycler as post-Accumulator should side-step the problem of reduced stacking rate when the Accumulator stack size increases above about 50 mA. Accounting for the increase in average stacking rate and assuming a negligible inefficiency in the process of transferring beam to the Recycler, an antiproton inefficiency of perhaps 32% would be sufficient to achieve the Run II goals. The increase in antiproton utilization efficiency is expected to arise from improved transmission through the Main Injector, from avoiding the inefficiency of coalescing the antiproton bunches,

* During the period October 1, 1994 to July 23, 1995 100.5 nb-1 of integrated luminosity was delivered to each of the two experiments and $1.91x10^{10}$ antiprotons were produced.

and from the recovery of unspent antiprotons by the Recycler at the conclusion of a Tevatron store.

For the purposes of the TeV33 design, we assume that the Run II goals will be met but that there will be no further increases in the antiproton utilization efficiency. Under these assumptions, the increase in luminosity is directly proportional to the increase in stacking rate, and we conclude that peak stacking rates of about 10^{12} antiprotons per hour are required to support two interaction regions at 10^{33} cm^{-2}-sec^{-1}. This rate is a 10-fold increase in stacking rate over the Tevatron I design, a 14-fold increase over the best stacking rate achieved, and a 5-fold increase over the projected Run II stacking rate. Clearly, dramatic increases in the antiproton production rate are an essential element of any plan to achieve a luminosity of 10^{33} cm^{-2}-sec^{-1} in the Tevatron proton-antiproton collider.

1.3 Importance of Beam-Beam Effect

The formula for the (linear) antiproton beam-beam tune shift with no crossing angle is:

$$\Delta\nu = 6\frac{r_p}{4\pi}n_c\frac{N_p}{\varepsilon_p} = 0.0073\ (\pi\,\text{mm-mrad}/10^{10})\ n_c\frac{N_p}{\varepsilon_p} \qquad [5]$$

where r_p is the classical proton radius ($1.535\text{x}10^{-18}$ m) and n_c is the number of interaction points. Operating experience in the Tevatron suggests that the maximum tolerable beam-beam tune shift lies in the range 0.02 to 0.025.

When the beam-beam tune shift is caused primarily by head-on interactions at zero crossing-angle, the beam-beam tune shift determines the maximum value of the factor N_p/ε_p, which appears in Eqn. [1]. For TeV33, the formula (Eqn. [5]) does not apply. In TeV33, the beams cross at an angle to avoid unwanted beam-beam interactions near the interaction region . The crossing angle at the interaction region dramatically reduces the beam-beam tune shift (some higher order effects increase), and the sum of the long range interactions cause tune shifts comparable to those at the interaction points. These crossing angle and long range effects depend on both N_p and ε_p separately, and may partially cancel depending on the detailed geometry of the beams and their orbits. These issues are discussed in considerably more detail in section 4.8. Despite the complicated nature of the beam-beam interaction, the proton beam parameters for TeV33 are consistent with a naive application of Eqn. [5].

1.4 TeV33 overview and parameters

The general strategy to increase the luminosity in the Tevatron proton-antiproton collider is to produce antiprotons at a much higher rate and to maintain the Run II antiproton utilization efficiency. This goal can be accomplished if the antiproton production rate can be increased and the emittances held at their Run II values. Some possible TeV33 parameters are given in Table

II. The antiprotons are distributed into more bunches (90 for TeV33 versus 36 for Run II). The number of bunches is determined primarily by the desire of the experiments to keep the number of interactions per beam crossing as low as possible. However, at least for the parameters shown in Table II, the number of bunches would have to increase to avoid excessive proton beam tune shifts (caused by high intensity antiproton bunches). The TeV33 parameters are, at this point, still speculative. It is quite possible that we will choose to obtain higher luminosity by making the bunches smaller in some dimension. One version (with improved rf focusing) is shown in Table II. For the parameters given, the bunch length is reduced from 35 cm to 15 cm and the form-factor is increased from 0.52 to 0.79. Other factors appearing in the luminosity formula can also be manipulated by various techniques. However, the *integrated* luminosity can be increased by at most a factor of 2 over the assumed antiproton utilization efficiency of 50%, because the integrated luminosity is limited by the production rate of antiprotons.

Table II. Possible TeV33 Parameters

Parameter	No Upgrades	rf upgrade	Units
Protons/bunch	27×10^{10}	27×10^{10}	
Antiprotons/bunch*	27×10^{10}	27×10^{10}	
Proton emittance (95%, norm)	20 π	20 π	mm-mrad
Antiproton emittance (95%, norm)	20 π	20 π	mm-mrad
Beam Energy	1000	1000	GeV
No. of Bunches	90	90	
Longitudinal Emittance	2	2	eV-sec
rf Frequency	53	212	MHz
rf Voltage	1	16	MV
Bunch length (rms)	0.37	0.14	m
Crossing Half-angle	0.17	0.17	mrad
Form Factor	0.36	0.72	
Typical Luminosity	0.8×10^{33}	1.7×10^{33}	$cm^{-2}sec^{-1}$
Number of IR's	2	2	
Bunch Spacing	132	132	nsec
Interactions per crossing	7.8	15.6	

*The maximum antiproton intensity is assumed to be equal to the proton intensity for the purposes of the luminosity calculation. Actual antiproton intensities will fluctuate from store to store.

2. Assumed conditions

2.1 Main Injector

The Main Injector is a project that will result in the replacement of the Main Ring by a smaller, larger aperture ring known as the Main Injector. The Main Injector project is nearing completion and is described in detail in the Main Injector Design Handbook.[2] Some of the major goals of the Main Injector project, relevant to TeV33 are listed in Table III. This document assumes that all of these goals will be met.

Table III. Main Injector Project Goals

Parameter	Goal	
Intensity per bunch	6×10^{10}	
Total Pbar production intensity	5×10^{12}	(84 bunches)
Proton beam transverse emittance	18π	mm-mrad
Proton beam longitudinal emittance	0.2	eV-sec
Main Injector transverse admittance (@8.9 GeV)	$40\ \pi$	mm-mrad
Main Injector longitudinal admittance (@8.9 GeV)	0.5	eV-sec
Coalesced bunch intensity	3×10^{11}	(per bunch)
Coalesced bunch transverse emittance	$18\ \pi$	mm-mrad
Coalesced bunch longitudinal emittance	2.0	eV-sec

2.2 Recycler

The Recycler is described elsewhere.[3] The most important design goal is to recover, on average, 50% of the antiprotons that could potentially be recovered. This goal could be met, for example, if 75% of the antiprotons are recovered from 75% of the stores that end normally[†]. We assume that we will continue to achieve the 50% antiproton recovery efficiency for TeV33 despite the increased number of bunches, the higher intensities, and (possibly) somewhat larger emittances.

The performance of the Recycler will be enhanced beyond the Run II goals that are described in Ref. 3. The electron cooling system will greatly increase the antiproton accumulation rate and the addition of a dedicated beam line between the Accumulator and the Recycler will enable frequent and reliable transfers to the Recycler.

2.3 Tevatron Energy

We have specified that the Tevatron will run at 1000 GeV in Run II and future runs. We have finished an upgrade to the cryogenic cooling system and have accelerated protons to 980 GeV. The plan to achieve 1000 GeV operation involves running some satellite refrigerators at lower pressure (and therefore a lower temperature) and some shuffling of magnets. It is clear that the ultimate energy limit of the Tevatron lies near 1000 GeV, but it is not clear whether we

[†] In Run Ib 71% of the stores were intentionally terminated. The others typically ended because of the failure of some critical component.

will be able to run reliably at 1000 GeV. The precise operating energy will depend on our success at optimizing the operation of the cryogenic systems (including possible improvements) and at mitigating the problem of low quench-current magnets.

2.4 Proton Removal

In order to recycle the antiprotons, they must be separated from the protons. We plan to eliminate the protons at the end of a Tevatron store, before deceleration. This plan has the advantage of making the deceleration process much easier because of the absence of beam-beam interaction effects. In addition, this scheme allows the deceleration of the antiprotons on the central orbit which has better field quality and more aperture than the helical orbit used for acceleration. However, the plan does require removal of the protons from the Tevatron at high field, when the Tevatron magnets have the least margin against quenches induced by beam loss. While we have substantial experience with removing the protons with scrapers for special experiments (the proton and antiproton beams are spatially separated), it typically takes half an hour to complete the process. Improvements both in technique and speed would be highly desirable. At the moment, it is uncertain how this goal will be accomplished in Run II.

The Tev33 parameters require the removal of about 3 times the number of proton bunches. The techniques established for Run II may require modification. We assume that an adequate solution will be found based on Run II experience.

3. Antiproton Production

The strategies for increasing the antiproton production fall into three categories:

1) Increase the number of protons targeted per pulse
2) Increase the proton beam pulse rate
3) Increase the antiproton collection efficiency

Relative to the Run II parameters, we plan to increase the number of protons targeted (by a factor of 1.9), to decrease the pulse rate by 25%, and to increase the antiproton collection efficiency (by a factor of 3.4), for a net increase in the antiproton flux of 4.8. The decrease in repetition rate is largely to allow more time per cycle for stochastic cooling although some decrease is required to accommodate the increased number of Booster cycles for slip stacking (see 3.1.3)

Table IV shows the numerology of antiproton production during Collider Run 1b and the production that would be expected in Collider Run II in the absence of upgrades to the target station, the injection line (AP-2), and the Debuncher apertures (assuming also that only a single Booster batch is targeted). The gain in production is due to the increased proton intensity on target and the increased repetition rate. Without the target sweeping system (described below), the yield (antiprotons produced per proton) would decrease because the proton beam spot size would need to be increased in order to keep the deposited energy density in the nickel target below 800 J/g. Assuming perfect Debuncher to Accumulator transfer efficiency, the maximum stacking rate in Run II will be 21.4×10^{10}/hour. In Run 1b, the Debuncher to Accumulator transfer efficiency was 80%, and the Accumulator stacking efficiency (rf stacking plus stack tail momentum cooling) was 90%. Upgrades to the Debuncher and Accumulator stochastic cooling systems are expected to increase these two efficiencies for Run II.

Table IV. Comparison of Run Ib and Run II antiproton source upgrades.

	Run 1b	Run II no upgrades
protons/pulse on target (10^{12})	3.2	5.0
cycle time (sec)	2.4	1.5
yield into Deb. ($\bar{p}$ /10^6 proton)	21.0	17.8
$\bar{p}$ /pulse into Deb. (10^7)	6.7	8.9
$\bar{p}$ /hour into Deb. (10^{10})	10.1	21.4
initial Deb. emit. (π-mm-mrad)	16.0	16.0

There are several upgrades which greatly increase the antiproton flux into the Debuncher in Run II and beyond:

1) Beam sweeping: By sweeping the proton beam in a small circle on the target during the 1.6 μsec spill, the energy deposition can be spread out over a larger volume of the target, and therefore the beam spot size can be made smaller, which increases the yield. The antiproton beam downstream of the target is then swept to remove the circular motion. In the absence of beam sweeping, each factor of 2 increase in proton intensity on target requires that the beam spot size be enlarged causing the antiproton yield to drop by 15-20%.
2) AP-2/Debuncher transverse aperture increase: The measured transverse emittance of beam entering the Debuncher is 15π x 16π, and the measured acceptance of the Debuncher is 29π x 26π. Increasing the AP-2/Debuncher transverse aperture to 32π x 32π will increase the yield into the Debuncher by a factor of 2.6.
3) Lithium lens improvements: Currently the lens operates at 750 T/m. Modest improvements to the original design may permit reliable operation at 900 T/m, which will increase the yield by 17% under current conditions.
4) Development of new lens design involving liquid lithium could allow reliable operation at 1200 T/m, with a further increase in yield. We are still investigating the feasibility of the liquid lithium lens.
5) Momentum aperture increase: The full momentum acceptance of the Debuncher is currently measured to be 4%. By ramping the slip factor η to .003 at injection, the momentum aperture can be increased by 18%, which increases the yield by 18%.

In addition to the above improvements, "slip stacking" in the Main Injector (longitudinally stacking more than one Booster batch of protons into the MI in each 120 GeV beam cycle) may

increase the integrated number of protons on target by a factor of 1.9 (see section 3.1.3). Table V summarizes the possible gains that can be made in antiproton production and collection with the above upgrades. The table lists the cumulative gains in yield and production. The order is arbitrary; the factors that increase the antiproton flux are largely independent.

Table V. Summary of antiproton yield and production improvements for TeV33

Upgrade	Factor	Yield into Deb. ($\bar{p}$ /10^6 proton)	($\bar{p}$ /hour into Deb. (10^{10})
Run II (without upgrades)	1.00	17.8	21.4
Beam sweeping	1.18	21.0	25.3
Slip stacking	1.90	21.0	48.1
32π x 32π	2.59	54.4	65.4
Debuncher Δp/p increase	1.18	64.2	124.5
Lithium lens to 900 T/m	1.11	71.3	138.2
Repetition Rate	0.75	71.3	103.6
Liquid lithium lens	1.09	77.7	113.0

While there are a number of techniques available to increase the antiproton flux, there is no realistic alternative to improved antiproton cooling. The plan for TeV33 requires higher frequency stochastic cooling in the 4-8 Ghz band and the introduction of electron cooling in the Recycler. The cooling is discussed in section 3.5.

3.1 Proton Intensity at the Antiproton Target

Increasing the intensity of the proton beam at the antiproton target is one technique to increase the antiproton flux. The higher intensity proton beam is difficult to accommodate in the target station because of the high peak energy deposition in the target, possible radiation damage to the target station components, and the need to shield personnel and the environment from excessive radiation. The TeV33 plan calls for an increase in proton intensity by a factor of 1.9 through the slip stacking technique described in section 3.1.3.

3.1.1 Linac & Booster performance

Run II specifications call for the Booster to produce 5×10^{12} protons per pulse with a maximum transverse emittance of 20π mm-mrad. The maximum Booster intensity achieved to date is 4.4×10^{12}, but the Booster normally operates at lower intensity in order to achieve the smaller emittance required by the Main Ring, where the effective normalized acceptance is about 13π mm-mrad. The Booster is expected to reach its goal of 5×10^{12} after a period of operation with the Main Injector.

Improvements in Booster intensity beyond those already expected would be useful in producing lower emittance proton beams in collisions and for producing antiprotons at a higher

rate. The Linac intensity is probably not of primary importance because beam can be injected for multiple turns using H^- ions. Most proposals for increased Booster performance involve fairly expensive Linac energy upgrades or construction of a larger aperture Booster to overcome space-charge effects. The more modest plans to improve the Booster aperture for Run II may be more effective than now anticipated. For the moment, it seems prudent not to rely on anything but incremental improvements in Booster intensity.

We now plan that the Booster longitudinal emittance will be 0.1-0.2 eV-sec for Main Injector operation, but the Booster appears to be capable of producing beams[4] of 0.07 eV-sec. Figure 1 shows the measured longitudinal emittance versus intensity in the Booster. The solid curve represents measurements taken with the old, 200-MeV Linac; the dashed curve was taken after the upgrade to 400 MeV. The improvement in longitudinal emittance is not the direct result of the 400 MeV upgrade, but the result of suppressing a longitudinal coupled bunch instability.

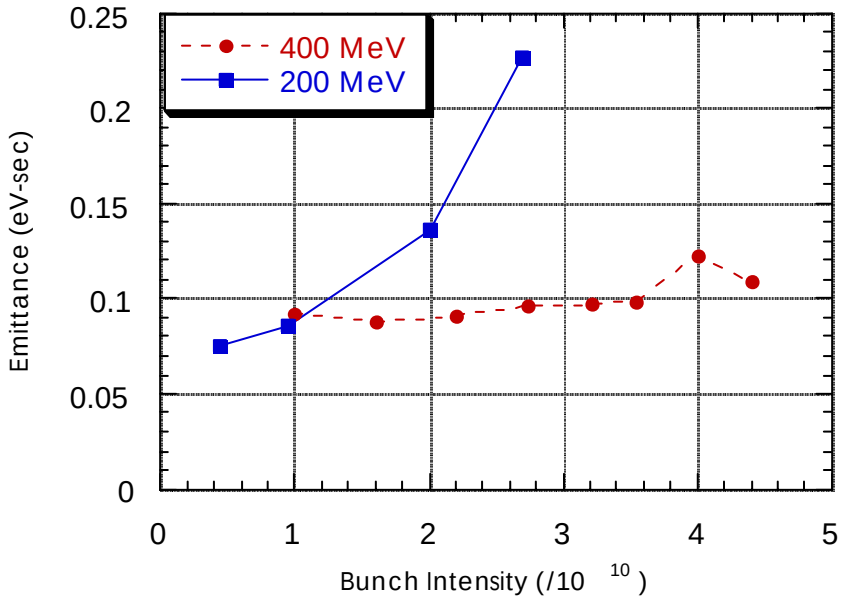

Figure 1. The Booster longitudinal emittance before and after the Linac upgrade.

3.1.2 Main Injector performance

The Main Injector was designed, in part, to accept the large emittance beams that one might expect on the basis of the extrapolation of the solid curve in Figure 1. We are left with the rather pleasant situation that the momentum spread of the Booster beam is considerably smaller than the momentum acceptance of the Main Injector. We expect to take advantage of the unexpected improvement in beam emittance by stacking multiple pulses into the Main Injector.

The ultimate Main Injector intensity limitation is not known either experimentally or theoretically. However, compared to the Main Ring, the Main Injector has a much larger aperture and more attention has been paid to achieving a low beam impedance. These features are expected to allow substantially higher beam currents. One known limitation is the amount of rf power available: the Main Injector can support 10^{11} particles per bunch without modification (the nominal design intensity is 6×10^{10}).

The Laslett tune shift for the Main Injector (space charge plus image charge) has been calculated (see reference 2) to be -0.08 for 6×10^{10} protons per bunch, but the maximum tolerable tune shift is unknown. The tune shift limit could possibly be increased with an improved resonance compensation scheme in the Main Injector, or the transverse or longitudinal emittances could be increased to decrease the tune shift. The increased emittances would have an effect on antiproton production (the effect of the longitudinal emittance on bunch rotation is discussed in section 3.4), but the emittance effects are weaker than the intensity effect.

Other collective effects, such as coherent beam instabilities, could make it difficult for the Main Injector to operate at higher intensities per bunch. We have extensive experience damping instabilities in the Main Ring and we should be able to damp dipole instabilities. Other instabilities, such as microwave type instabilities, could be more difficult to handle.

3.1.3 Slip stacking

The most promising strategy to increase the beam intensity seems to be to stack Booster pulses in the Main Injector. The most promising technique appears to be to coalesce bunches in the Main Injector with a technique known as "slip stacking". Slip stacking is particularly attractive because it requires no major hardware and could be implemented at the *beginning* of Run II. A cartoon of the stacking process is shown in Figure 2. A similar technique has been used at the CERN Proton Synchrotron (PS).[5]

According to the current plan for Run II, the 120 GeV protons used in antiproton production will be obtained by transferring one Booster batch into the Main Injector at 8 GeV and accelerating it to 120 GeV. The proton intensity can be nearly doubled using 'slip stacking' in the Main Injector. This involves stacking two Booster batches end to end, but with slightly differing momenta, into the Main Injector. The two batches have different periods of revolution and 'slip' relative to each other azimuthally and finally overlap. When they overlap they are captured using a single rf which is the average of the initial frequencies associated with the two batches. Since the Booster and Main Injector acceleration cycles are 66 ms and 1.5s respectively, the need for an extra Booster cycle increases the total antiproton production cycle by less than 0.1 sec and is a small effect on the total cycle time. We have planned for the TeV33 production cycle to be 2.0 sec. This cycle time is long enough to load the Main Injector with 6 Booster batches, slip stack one batch (to be used for antiproton production) and to extract the other 5 batches for fixed target experiments. Slip stacking on all 6 batches (12 Booster cycles) is, in principle, possible, but requires a longer Main Injector cycle.

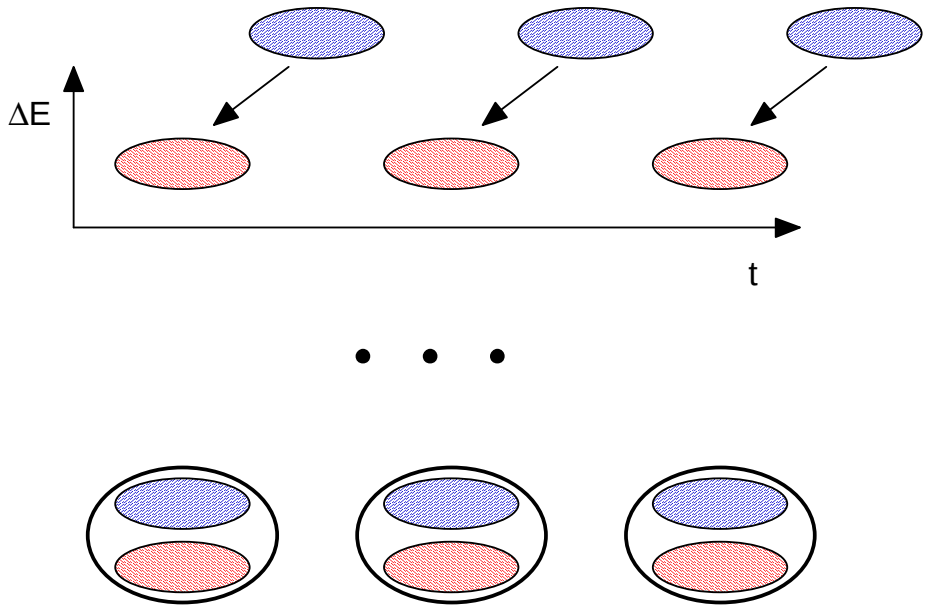

Figure 2. A cartoon of slip stacking. Two batches of beam are displaced in azimuth and energy (above), are brought close to each other, and are then combined in a single, large bucket.

The following is a list of factors that determine the optimum momentum separation between the two batches, initially and before they are coalesced, and the rf voltages involved.

1) A larger momentum separation reduces the time before the batches can be coalesced.
2) A larger momentum separation requires a larger horizontal aperture.
3) A smaller momentum separation just before the batches are coalesced leads to a smaller longitudinal emittance for the final beam (neglecting the effect of the second rf system).
4) The rf buckets for the two batches get more distorted as the separatrices move closer together. The losses become fairly high if the separatrices overlap. So the beams should spend as little time with their separatrices close together as possible before they are coalesced.

The procedure used to find a way to obtain a final coalesced beam of small emittance containing a reasonably large fraction of the initial beams, consists of two steps. The first step, described in more detail in section 3.1.3.1, consists of finding the approximate heights of the initial buckets and that of the final bucket after coalescing, which would result in a final beam of small longitudinal emittance with small losses during coalescing. We ignore the distortion of the rf buckets due to multiple frequencies in this step. In the next step, which is described in section 3.1.3.2, we use these approximate heights of the buckets as starting points and use rf simulations that include the distortion of the buckets, to find an acceptable strategy of rf manipulations to achieve our goals and to estimate the final emittance of the beam and the losses during coalescing when we use the strategy.

In Section 3.1.3.3 we estimate the effects of beam loading and consider ways to overcome its adverse effects. The effects are serious due to the high intensity of the proton beam. Compensating for the effects is complicated by the simultaneous presence of two beams and rf systems.

3.1.3.1 Optimum rf bucket heights

The optimum bucket heights before and after coalescing were found assuming gaussian particle distributions for the initial beams. The harmonic number is 588 and rf frequency is approximately 53 MHz respectively. We assume a 0.15 eV-s longitudinal emittance for each of the initial beams. This value is the measured emittance in the Main Ring at injection. The emittance in the Main Injector is expected to be lower due to improved Booster performance. The height of a bucket with area 0.15 eV-s is 6.15 MeV.

For given heights of the initial and final buckets after coalescing, the area of the beam contour in the final bucket containing 95% of the initial beam was found by integrating the part of the initial gaussian distribution within the contour. The process was repeated for various heights of the final bucket. Figure 3 shows the area corresponding to various final bucket heights, for an initial bucket height of 6.2 MeV. The height that gave the minimum area was chosen as optimum final bucket height for the given initial bucket. The process was repeated for various values of the initial bucket height. Figure 4 shows the optimum final bucket heights and the heights of the corresponding beam contours containing 95% of the beam for various initial bucket heights. Figure 5 shows the minimum area containing 95% of the beam for various initial bucket heights.

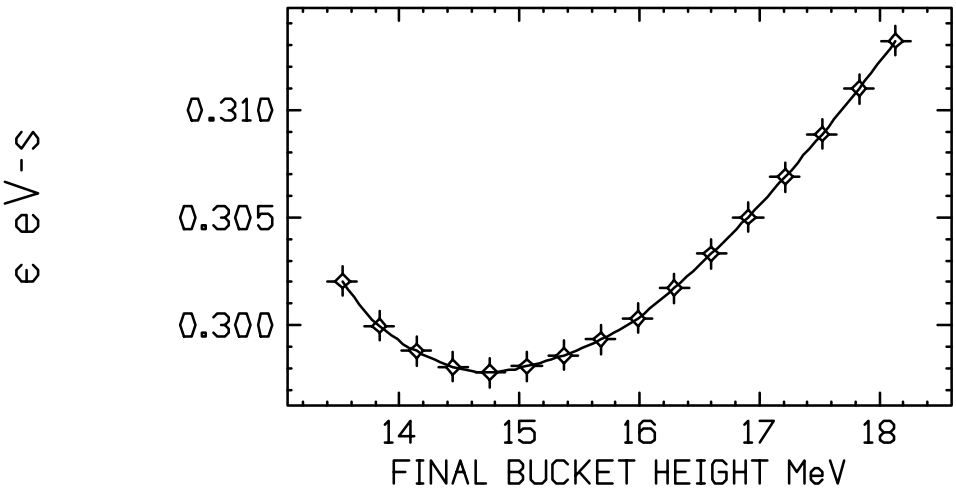

Figure 3. Area containing 95% of beam vs final bucket height for an initial bucket height of 6.2 MeV.

Even if the injected beams are gaussian, the beam distributions before coalescing are not expected to be gaussian if the two rf systems have frequencies that are close together. The distortion of the distributions due to the presence of the second rf was determined using a tracking simulation and is described in section 3.1.3.2.

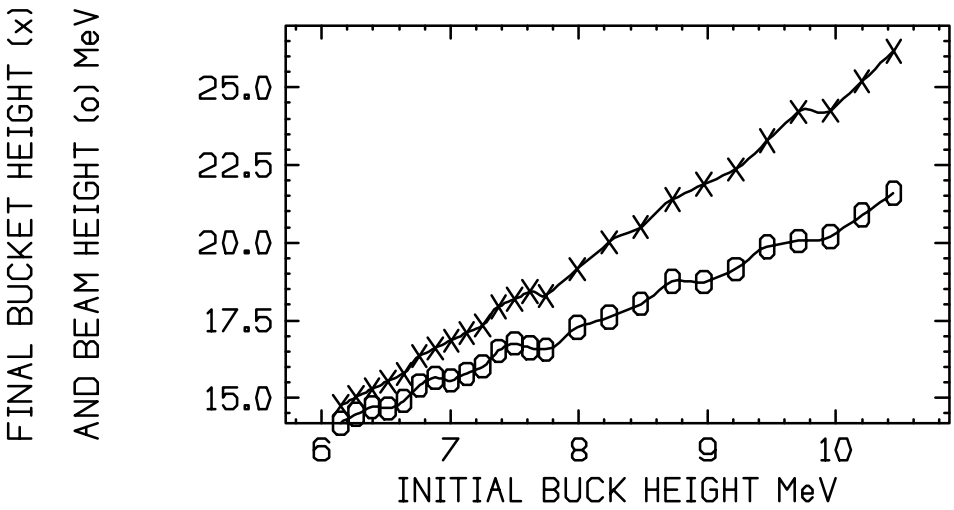

Figure 4. Optimum heights of the final bucket and the beam for various heights of the initial bucket.

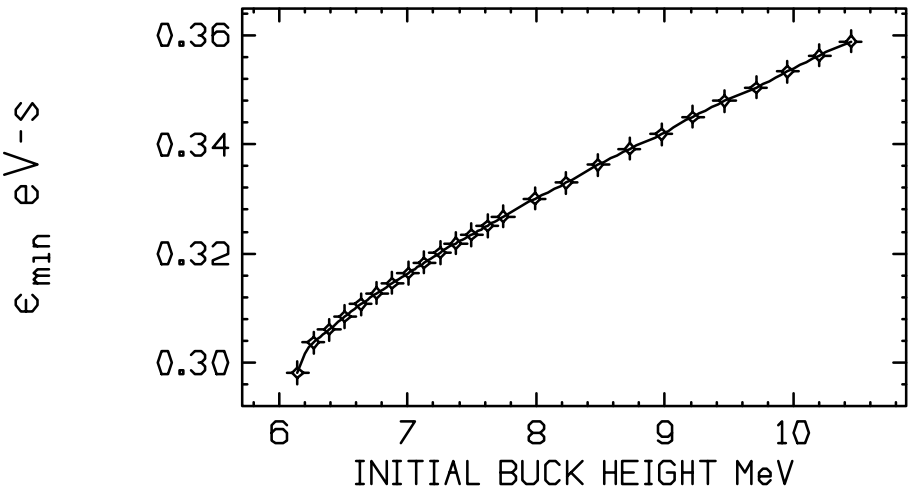

Figure 5. Minimum area containing 95% of beam for various heights of the initial bucket.

3.1.3.2 Acceleration and Coalescing

The fractional difference in periods of revolution for the two batches is given by

$$\frac{\Delta T}{T} = \eta \frac{\Delta p}{p}, \qquad [6]$$

where $\Delta p / p$ is the fractional momentum difference and η is the slip factor. The slip factor is given by

$$\eta = \frac{1}{\gamma_t^2} - \frac{1}{\gamma^2} \qquad [7]$$

For the MI, $\gamma_t = 21.8$, $\gamma = 9.55$ at injection , and $\eta = 8.86\times10^{-3}$. The length of a Booster batch is 1.57 μs, and the period of revolution in MI, T = 11.14 μs at injection. If the two batches are injected 46 MeV apart and allowed to slip, they would overlap completely after half a Booster cycle, i.e., 33 ms. Simulations show that for a bucket height of 10 MeV, the distortion of the particle distributions due to the presence of the second rf is negligible. However, to obtain a small longitudinal emittance of the final beam, the two beams have to be accelerated towards each other before they are coalesced. The bucket height has to be reduced so that the two beams can be brought close together. Were it not for the effect of the second rf one could accelerate the beams and reduce the bucket height very slowly to minimize particle loss. The presence of the second rf encourages faster rf manipulations once the beams are close to each other.

The rf curve program was determined by trial and error. After a few trials, the variation of the rf voltage, frequency, and synchronous phase angle depicted in Figure 6 was accepted as satisfactory. The two beams are captured with a single rf while they are still accelerating. The efficiency of acceleration and coalescing for a final longitudinal emittance of 0.34 eV-s is 95%. Figure 7 shows the beam distributions just before coalescing along with the initial and final buckets. The dashed curve inside the final bucket is a contour containing 0.34 eV-s of area.

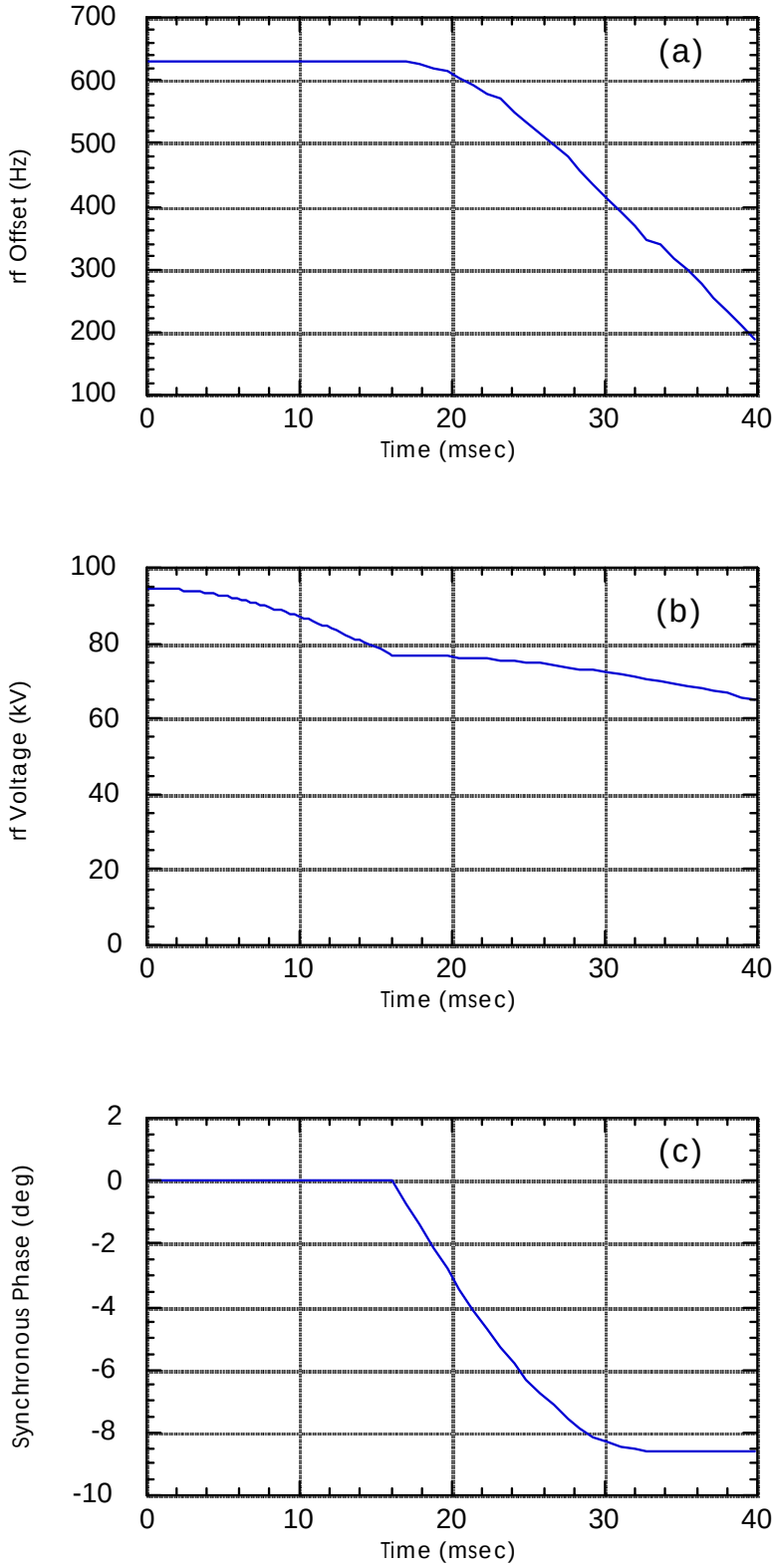

Figure 6. The frequency curve (a), the voltage curve (b), and the resulting synchronous phase angle (c) that were used in the tracking simulation.

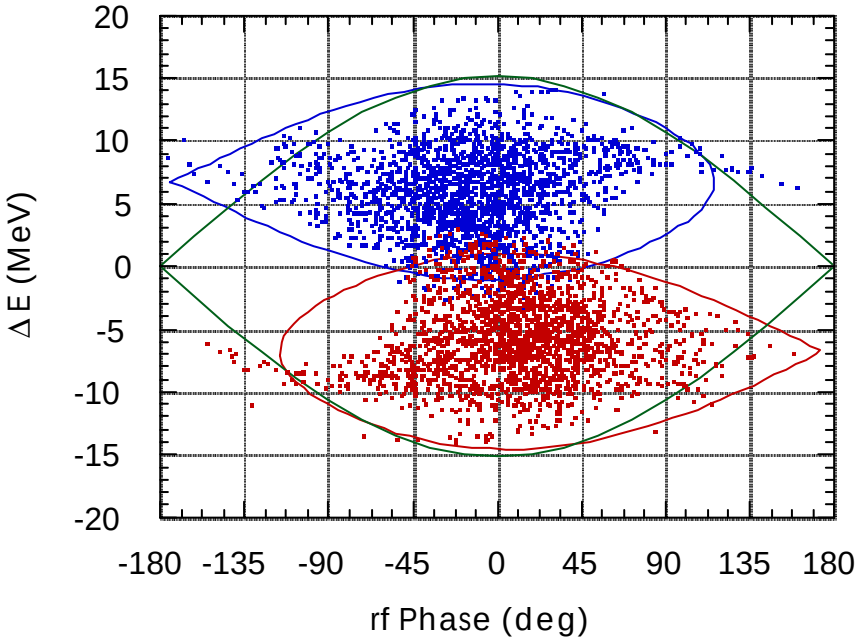

Figure 7 A simulation of slip stacking. The points represent the final phase space coordinates of the particles tracked in the presence of the two rf systems. The smaller curves are the moving rf buckets that would be generated by one system if the other system were not present. The large curve represents the stationary bucket into which most of the particles will be captured.

3.1.3.3 Beam Loading

Because of the high beam current, the beam loading voltage in the rf cavities is a serious concern. If the quality factor, Q, is high and the bunch length is short, the cavity voltage $V(t)$ following the passage of a bunch of charge q is given by:

$$V(t) = \frac{q\omega_r R}{Q} e^{-(\alpha+i)\omega_r t} \qquad [8]$$

where R is the cavity shunt impedance, ω_r is the cavity resonant frequency, and α=1/2Q. In the case that the bunches are spaced by τ=2π/ω_r, the voltage after the passage of n bunches is easily found to be

$$V(n\tau) = \frac{q\omega_r R}{Q}\frac{1-e^{-n\pi\alpha}}{1-e^{-\pi\alpha}} \qquad [9]$$

We can apply Eqn. [9] to estimate the beam loading voltage. As an example, we consider the case where there are two batches of 84 bunches each in the Main Injector and that the last 42 bunches of the first batch and the first 42 bunches of the last batch overlap and are exactly in phase. We ignore the difference in revolution frequencies of the two batches and the difference between the resonance frequency of the cavity and the revolution frequencies. Under these circumstances, one can use a generalization of Eqn. [9] to estimate the beam loading voltage as shown in Figure 8. The beam loading varies dramatically as the bunches slip past each other. When the bunches from the two batches are in phase (0° curve in Figure 8), the beam loading voltages add. But when the bunches are out of phase (180° curve in Figure 8), the beam loading voltages nearly cancel. The calculation is for a total of 18 cavities with R/Q=100 Ω and Q=5000. The voltage increases when the beam passes through the cavities. During the time that the two beams overlap the voltage increases at twice the rate. When the beam is absent the voltage decays at a rate determined by the time constant α. Approximately 0.4 ms later the bunches are out of phase and the beam voltage becomes very small.

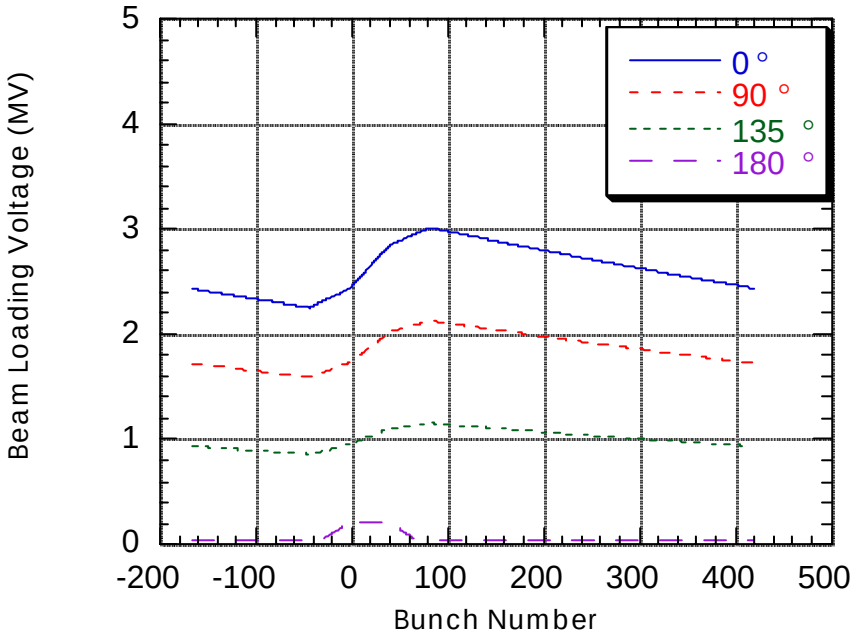

Figure 8. A calculation of beam loading for the point at which the two Booster batches partially overlap (by 42 out of 84 buckets). The various curves show the variation in beam loading voltage as the rf phase between the two batches varies from 0° to 180°.

This estimate of the beam loading voltage indicates that, if uncompensated, the beam loading voltage (3 MV) would dwarf the rf voltage (100 kV). We propose to control the beam loading voltage by:

1) Tuning all cavities to the nominal 8 GeV frequency.
2) Using a small number of cavities (2 or perhaps 4) to produce the required rf voltage and de-Qing the remaining cavities. One simple technique that appears to be moderately effective is to turn off the screen voltage to reduce the tube plate resistance. This technique is estimated to de-*Q* the cavities by a factor of 3.
3) Feed-forward can be used on all the cavities. A resistive gap measures the wall current. This current, after being properly scaled, can be applied to the cavity drivers. Based on current Main Ring experience it is expected to achieve a factor of 10 reduction in the beam loading.
4) Feedback can be used on all the cavities. A signal proportional to the gap voltage is amplified, inverted, and applied to the driver amplifier. This technique is expected to achieve a factor of 100 reduction in beam loading voltage (based on previous experience in the Main Ring and results achieved elsewhere).

If all these efforts were successful, beam loading should be reduced to a negligible value. Experiments in the Main Ring to measure the suppression of the beam loading voltage and calculations of the tolerance of the slip stacking process to large beam loading voltages will determine the feasibility of slip stacking in the presence of relatively high impedance rf cavities.

Other collective effects could be important. These include:

1) Microwave instabilities at low voltages
2) Feedback loop coupling
3) Cavity tuning instabilities

We plan further theoretical work and are beginning experimental work using the Main Ring beam.

3.2 Antiproton Target

The higher intensity proton beam expected at the antiproton target in Run II and TeV33 results in an increasingly hostile environment at the target station. Run II doubles the amount of beam targeted compared to Run I; TeV33 results in a further doubling of the intensity. The antiproton source target area is a high radiation area that contains a number of high voltage devices.

3.2.1 Beam sweeping

One issue that is fairly well understood is the allowable peak energy deposition in the target. Figure 9 shows the relative yield of antiprotons as a function of rms beam spot size. Also shown is the energy density in a copper target as a function of rms beam spot size as calculated by MARS10[6] for 5×10^{12} protons per pulse[7]. Estimates of the peak density of energy deposition per pulse achieved to date are in the range of 800 J/g. This is above the melting point of copper (about 600 J/g), and close to the melting point of nickel (about 1000 J/g). In order to maintain

peak energy deposition below present levels the spot size would have to be increased to 0.3 mm for Run II (5×10^{12} protons in a 1.6 μs pulse) and the yield would be reduced 15-20% compared to the nominal beam size of 0.10-0.15 mm. We plan instead to sweep the beam on the target while synchronously sweeping the downstream acceptance so that we can obtain an effective defocusing of the beam with no reduction in yield.[8] With slip stacking, the sweeping radius will need to be increased to about 0.5 mm. The current design of the beam sweeping system is compatible with a maximum sweeping radius of 0.5 mm, but uncertainties such as the breakdown voltage of the magnets in the beam environment may limit the maximum sweeping radius to the design value of 0.33 mm.

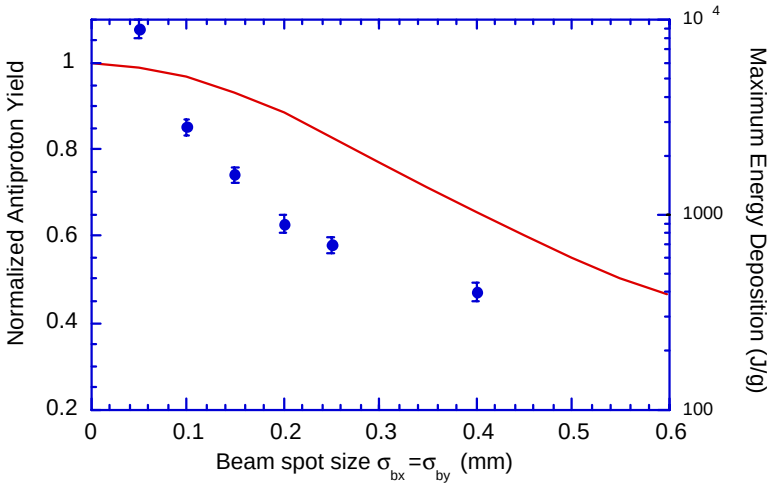

Figure 9. Yield (line) and energy deposition (points) for 5×10^{12} protons versus beam spot size

The beam sweeping scheme utilizes two upstream sweep magnets driven in quadrature by a 625 kHz sinusoidal current wave-form to trace a circular pattern on the target with the 120-GeV proton beam, followed by two downstream magnets to redirect the 8 GeV antiprotons exiting the collection lens parallel to the AP-2 transport line (see Figure 10). The sweeping radius is much smaller than the 2 cm diameter of the lithium collection lens and the aperture of AP-2. Two current-carrying plates, roughly 3 cm wide, with an air gap of 3 cm, will provide the deflecting magnetic field. An air gap is used since the beam is already transported through air from upstream of the target to downstream of the pulsed magnet. This system is currently an R&D project with expected completion of a prototype kicker magnet and power supply in late 1997.

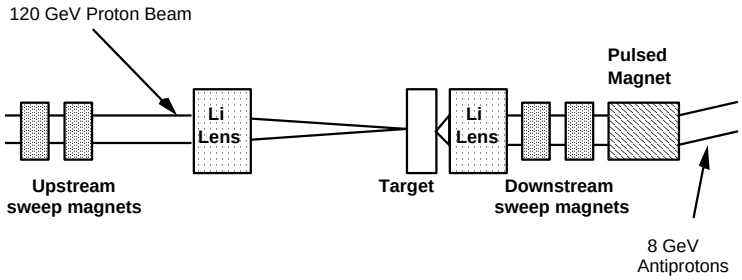

Figure 10. Target station layout showing beam sweeping kicker magnets

3.2.2 Lithium lens mechanical issues

The collection lens[9] focuses the antiprotons produced at the target. The effect of the lens gradient on the yield is discussed in section 3.3.1. However, because the lithium lens is subject to the hostile environment encountered in the target station, reliability issues are discussed here. The current-carrying lithium portion has a diameter of 2 cm and a length of 15 cm. The lithium is encased in a cylindrical water-cooled Ti-6Al-4V jacket. Fermilab lithium lenses of recent design have survived over 7 million pulses at a lens gradient of about 750 T/m. Increasing the field gradient of the lens increases the yield. But even a small increase in repetitive stress in the Ti-6Al-4V cylinder (which acts as both a cooling jacket and a pressure vessel) leads to a much shorter fatigue life of the metal. Thus, operation at even 5% greater field gradient has not yet proven possible beyond 1-2 million pulses. Several improvements in the design of the lens are expected to further improve reliability and field strength. Our ultimate goal is to improve the current design to be reliable at 900 T/m. A number of improvements to the mechanical design have been developed already. These improvements include thicker end caps for the cooling jacket, a stronger beryllium window, and improved handling and placement of welds during construction of the cooling jacket. These improvements have been incorporated into the latest lenses, which have been tested extensively in the target vault at 750 T/m. These lenses will be tested at higher lens field gradients in the future.

One particular critical parameter is the lens preload. During the filling process, lithium is pumped under pressure into the evacuated titanium vessel. The preload serves to insure that the lithium cylinder maintains its shape at mid-pulse, when significant magnetic pinch forces are present. Lower preload leads to lower operating stresses; a small stress decrease on the titanium cooling jacket should result in a great increase in the life of the lens for a given field gradient. A recent analysis using ANSYS[10] shows that it is possible to lower the preload pressure in the lithium by at least 15%. The original lens design preload ensured that the lithium would maintain its shape on the first pulse when the lithium is at 20 ˚C. In its steady state, the lens is at 65 ˚C and the additional thermal stress on the titanium is approximately the same as the stress due to the preload. Thus, at steady state almost no preload is needed. If one could reduce the lithium preload from 2300 psi to 500 psi, then the lens would be able to operate at 1000 T/m

without deformation of the lithium cylinder. A lens with a preload of 1950 psi is currently in use in the target vault.

Lithium melts at the relatively low temperature of 180 ˚C. If liquid lithium were used in the lens and circulated through a heat exchanger with a pump, then water cooling of the Ti jacket would not be necessary. This would allow for a much more robust Ti jacket that could withstand much larger shock waves, allowing for larger current pulses and magnetic field gradients. Some R&D has been done in this area in the past.[11] Gradients of 1200 T/m might be possible with this technique.

3.2.3 Radiation damage issues

Information on the maximum allowable radiation dose of insulating materials is sketchy, but we already typically exceed the high end of the ranges specified. Because of the large uncertainty in using published data, the final determination on the acceptability of materials for use in our target station will necessarily be based on our own experience. Recently, a failure of the torlon® insulating material in the "pulsed magnet" was experienced. This material had survived a 4-year beam exposure at current intensities. Higher beam intensities will result in accelerated failure rates or will further restrict the range of materials that can be used in the target vault.

We have seen a large number of lithium lens failures over the years. Few, if any, of these failures were the result of radiation damage. However, we have realized that the lithium lens is susceptible to a type of radiation damage that is unique to the lithium lens. Gaseous products from the reaction $^{6}\mathrm{Li} + n \rightarrow {}^{3}\mathrm{H} + {}^{4}\mathrm{He}$ are expected to build up over time, possibly affecting the operation of the lens.[12] Swelling of the lens is expected, due to the pressure of the contained gas, potentially limiting the lifetime of the lens under an intense beam environment. To avoid this problem, we have identified a source of 99% isotopically pure ^{7}Li and are currently building all lenses with this material.

While there are no problems that have been identified as being insurmountable, the susceptibility of target station components to radiation damage remains a concern based on our past experience. In our plans for TeV33, we have chosen to achieve some of the required increase in antiproton flux by increasing the antiproton acceptance. This strategy helps reduce the potential for radiation damage (compared to the scenario where all the increase is achieved by targeting more protons), but it does require higher performance from the stochastic cooling systems.

3.2.4 Antiproton target radiation shielding and environmental issues

The radiation shielding and environmental issues are fairly well understood. Higher beam intensities will probably require modifications to the shielding or to the accessibility of the target hall. It is likely that improved air handling procedures (to reduce airborne contamination) will also be required. Some of the major concerns are listed below.

1) The target vault is classified as a high radiation area (<100 mrem/hr). Some additional concrete may be required to maintain this classification (a standard rule of thumb is that 2.3 ft of concrete reduces the dose rate by a factor of 10).[13]

® Torlon is a registered trademark of Amoco Corporation.

2) The AP0 building is classified as a radiation area (<10 mrem/hr). Some additional concrete shielding may be required to maintain this classification. As an alternative, some critical areas could be enclosed by ropes or fences.
3) The lithium lens is cooled by a closed loop water system. The levels of tritium may require additional measures to comply with established safety standards.
4) Stairwells and penetrations have not been considered in detail, but may need some additional shielding measures.
5) Some additional soil may be required over the beam lines.
6) The ground water contamination potential has been considered with the "Concentration Model."[14] The result of the calculation based on this model is that we can target 10^{22} protons per year in the existing antiproton target station. This is well within the TeV33 parameters of 10^{7} pulses of 10^{12} protons per pulse.
7) The limit on airborne emissions is 100 Ci per year. The measured[‡] target station emissions indicate that 10^{20} protons per year will saturate the 100 Ci limit.

3.2.5 Antiproton Target Conclusions

In summary, our current understanding is that targeting twice the Main Injector intensity (*i.e.*, 10^{13} per batch) is technically feasible provided that the beam sweeping system operates reliably.

3.3 Antiproton Acceptance

We plan to increase the antiproton yield by increasing the gradient at which the lithium lens can reliably operate and by increasing both the transverse and longitudinal acceptance in the Debuncher. Increasing the acceptance has the advantage that it makes no new requirements on the proton beam and target station components, but it has the disadvantage that a larger phase space area must be cooled.

3.3.1 Lithium Lens Gradient

Measurements of yield vs. gradient (Figure 11) show that the yield increases approximately linearly over the range measured. These yield data were obtained with the current acceptance, which has been measured to be about $16\pi\times16\pi$ mm-mrad with the AP-2 line matched to beta functions β_x=2.5 m and β_y=1.5 m at the downstream focal point of the lithium lens. We have established a goal of 900 T/m for the improved lithium lens design (as described in section 3.2.2), which would result in a 17% increase in yield if everything else remained the same. However, if the acceptance is increased to $32\pi\times32\pi$ mm-mrad and the AP-2 match is reoptimized to $\beta_x = \beta_y$=4.5 m, we calculate a 28% increase in yield for the same increase in lens current using the Monte Carlo computer program MCLENS[15]. We plan to achieve the latter increase in yield with improvements to the AP-2 line and the Debuncher Ring.

[‡]In 1995 (a collider run) 15×10^{18} protons were targetted and 19 Ci were released.

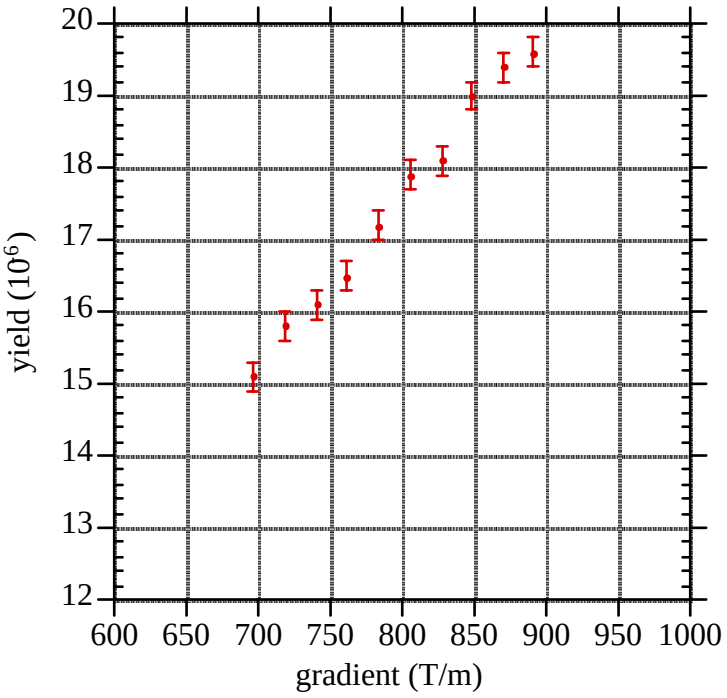

Figure 11. Measured yield vs. lithium lens gradient

3.3.2 **Transverse aperture increase to 32π x 32π**

The transverse phase space area of antiprotons accepted into the Debuncher during stacking has been measured to be about 16π x 16π (see Figure 12). This is substantially smaller than the measured admittance of the Debuncher of 29π x 26π, and we have suspect that the AP-2 beam transport line may be limiting the acceptance. The apertures in the AP-2 line are large enough for a 32π x 32π beam but the acceptance could be limited by misalignment of the apertures, beam steering, or focusing errors. These types of errors are coupled. We suspect steering errors are partially compensated by changing quadrupole gradients (which results in focusing errors). Recently, the quadrupoles in the upstream end of AP-2 were surveyed and realigned in an effort to minimize quadrupole steering, but no increase in yield was observed. Work is presently underway to develop an accurate beam line model and improve the beam line tune, steering, and matching into the Debuncher.

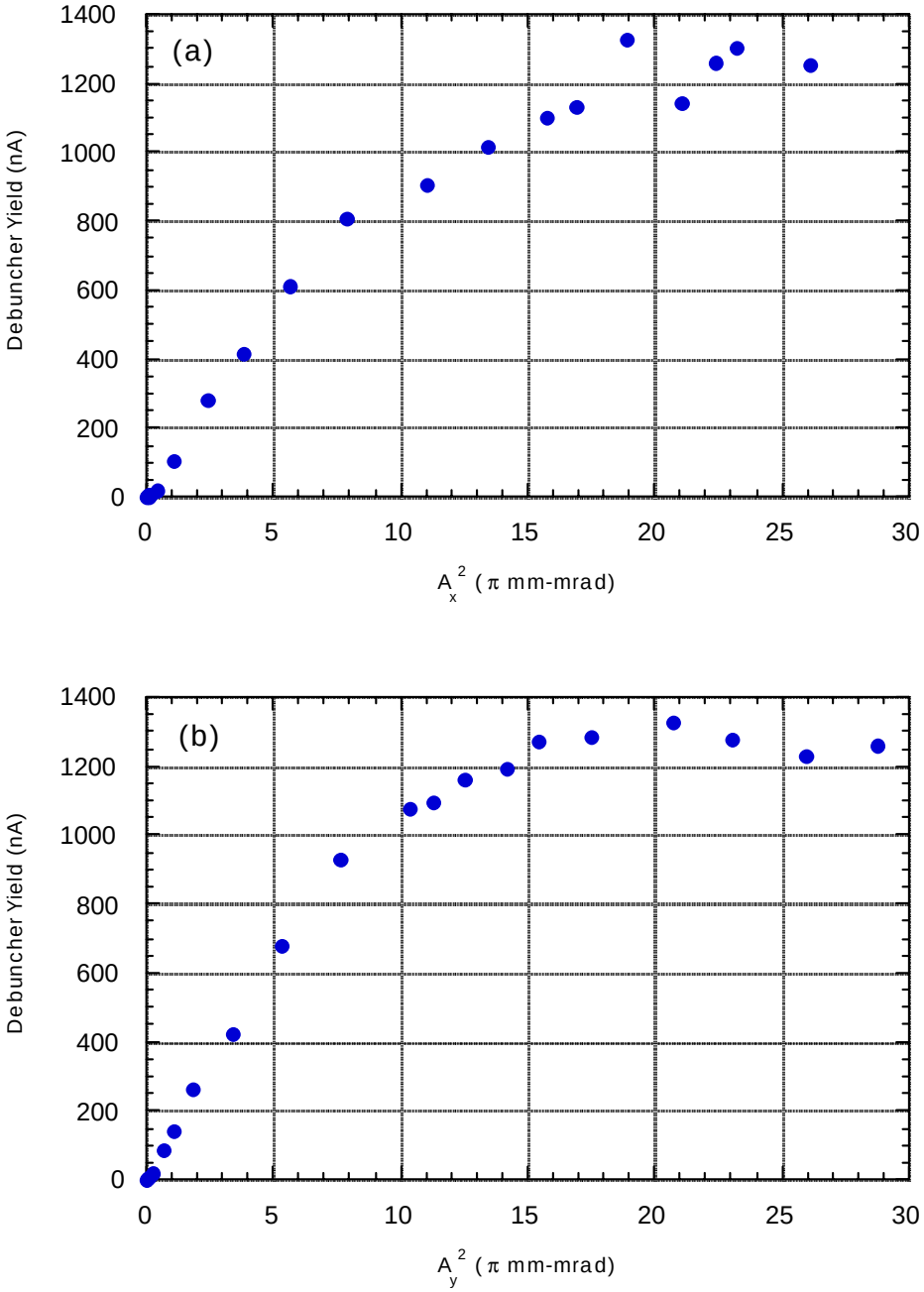

Figure 12. The transverse phase space area of antiprotons circulating in the Debuncher is deduced by measuring yield versus transverse scraper position and using $A^2=\Delta x^2/\beta$. The yield is shown as a function of horizontal (a) and vertical (b) acceptance. The Debuncher Yield is defined as the circulating current in the Debuncher (590 kHz revolution frequency) per 10^{12} targeted protons. At the location of the scrapers, β_x=13.1m and β_y=13.9m.

3.3.3 Matching the Beam Phase Space to the Debuncher Admittance

Figure 13 shows a Monte Carlo simulation (see Ref. 15) of the antiproton phase space density in the horizontal dimension at the downstream focus of the lithium lens. A fit to the measured yield vs. target-to-lens distance indicates that the aspect ratio of the phase space ellipse at the lens which is accepted into the Debuncher is now β=2.5 m horizontally and β=1.5 m vertically.[16] However, for apertures up to about $32\pi \times 32\pi$ and for a lens gradient of 750 T/m the optimum phase space ellipse (maximum yield) is β=4.5 m in both dimensions. If the $32\pi \times 32\pi$ mm-mrad acceptance is achieved and if AP-2 is optimally matched to the Debuncher, the yield is predicted to increase by a factor of 2.59 at the current lens gradient of 750 T/m. A major uncertainty in this extrapolation is the assumption that the current acceptance is an ellipse centered in phase space. (It might not be centered.) Figure 14 shows the beam envelope for 32π x 32π beam, initial $\beta_{x,y}$=4.5m, and $\Delta p/p$=4% in an AP-2 model. This model (assuming perfect steering) shows that the beam easily fits in the AP-2 beam pipe, except possibly at the injection septum. The narrowest apertures are horizontally at the upstream end of the septum (4.2 $\times$ beam sigma), vertically at the downstream end of the septum (6.5 $\times$ beam sigma), and horizontally at the upstream end of the injection kicker (6.7 $\times$ beam sigma).

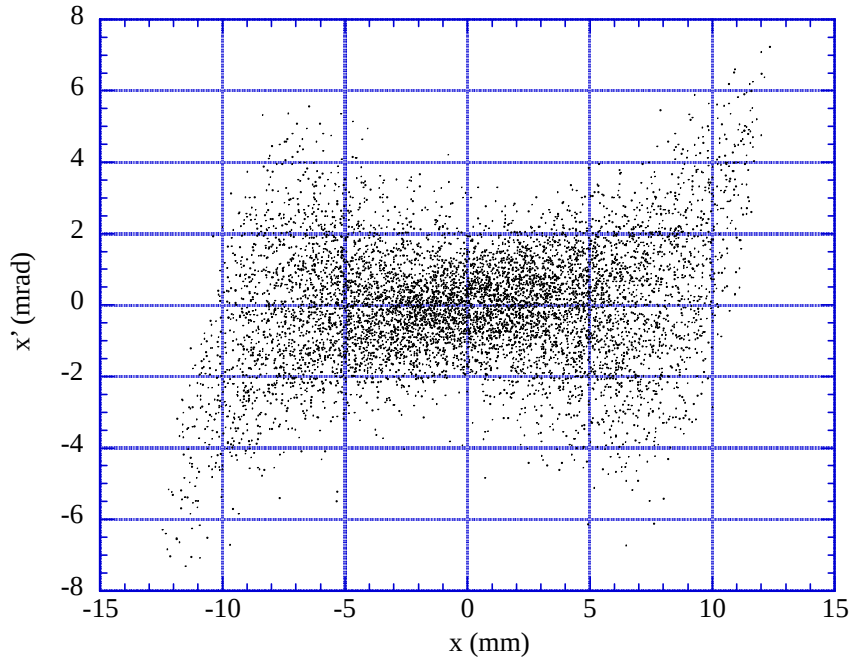

Figure 13. Calculated phase space density at the downstream focus of the lithium lens with a lens gradient of 750 T/m. The corresponding vertical distribution is the same because of the cylindrical symmetry of the beam and the lithium lens.

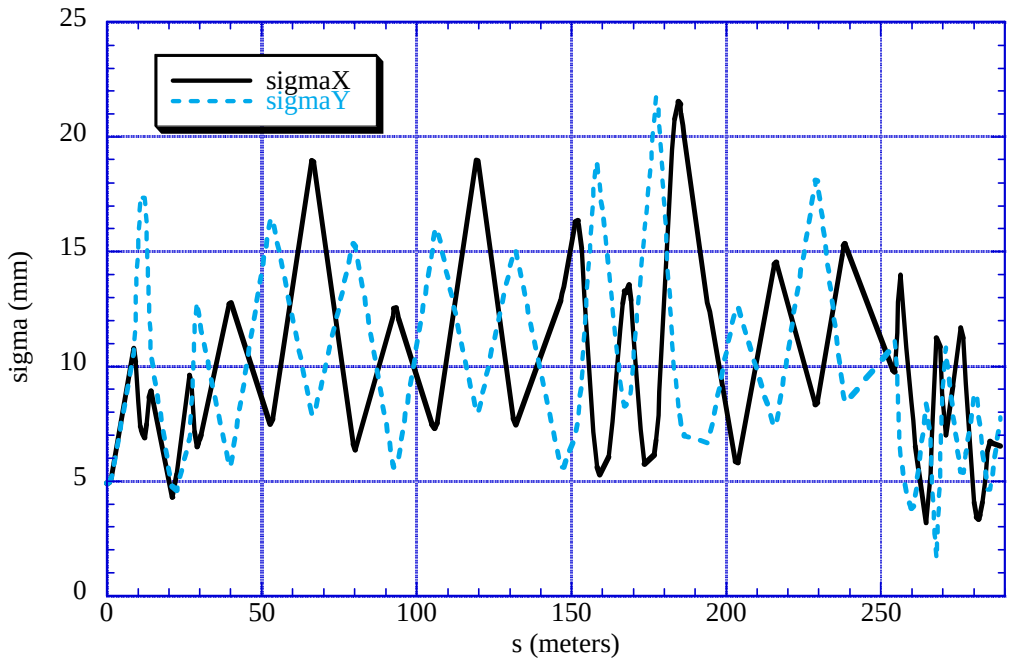

Figure 14. Vertical and horizontal beam envelopes in AP-2 based on model with 32π x 32π beam, initial $\beta_{x,y}$=4.5m, and Δp/p=4%. Left side of figure is downstream focus of lithium lens, and right side of figure is downstream end of Debuncher injection kicker magnet.

3.3.4 Debuncher Aperture

The Debuncher transverse aperture has been measured to be as large as 29π x 26π mm-mrad at the central momentum[§] although it generally deteriorates with time to something more like 25π x 23π mm-mrad. Aperture scans indicate aperture limitations at the stochastic cooling pickup and kicker arrays. The Debuncher stochastic cooling upgrade for Collider Run II will increase the aperture of these devices to a nominal 40π mm-mrad. Previous measurements[17] indicated that even with the cooling tanks removed, the apertures were still limited to about 29π mm-mrad. The Debuncher model indicates (ignoring steering , focusing, and alignment errors) that without the cooling tanks, the aperture is greater than 40π everywhere except at the extraction kicker (A_y=36π) and the injection septum (A_y=29π). A stronger injection kicker would allow for a greater separation between the circulating beam and injected beam at the downstream end of the septum. Then, bumping the closed orbit away from the septum would allow for a vertical aperture larger than 40π at that point. The issue of whether or not new kickers are required needs more careful study. A further possible cause of the limited aperture is quadrupole misalignment, which causes beam steering, which cannot be corrected because there are very few correction elements in the bend sections of the Debuncher. Figure 15 summarizes a

[§] The Debuncher transverse aperture is smaller at values of Δp≠0. In yield calculations it is assumed that if the transverse aperture at Δp=0 is increased by a multiplicative factor, the aperture at Δp≠0 will increase by that same multiplicative factor.

recent Debuncher quadrupole survey. These alignment errors are large compared to the original survey tolerances, but their effect on the beam has not been studied in any detail. These elements will be realigned during the long shutdown for Main Injector installation. If this does not open up the aperture, then a program of installing motorized quadrupole mounts, dipole shunts, and possibly trim elements in conjunction with beam-based alignment techniques may be appropriate to obtain an acceptance of $32\pi \times 32\pi$ mm-mrad. Beam studies with the goal of defining the program to increase the acceptance of the AP-2 line and Debuncher are currently underway.

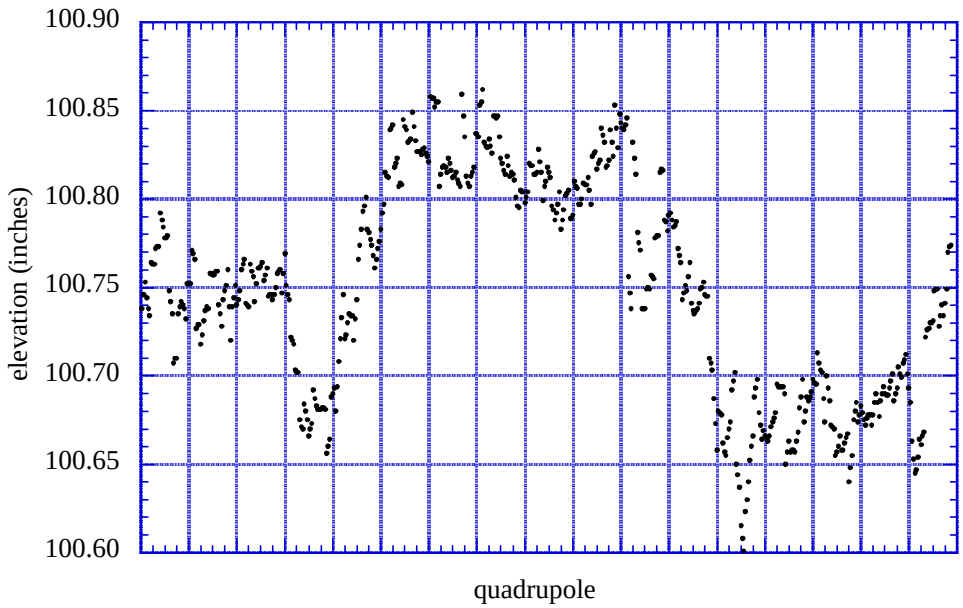

Figure 15. Quadrupole vertical misalignment in the Debuncher Ring. Each quadrupole was surveyed at its upstream end and downstream end.

3.3.5 Momentum aperture increase

By decreasing the slip factor η in the Debuncher from its design value of .006 to .003 at injection time, the momentum aperture of the Debuncher can be increased by 17% at injection. This is accomplished by reducing the dispersion in the bend sections of the Debuncher. Figure 16 shows the dispersion function in the Debuncher for 2 different values of η. The η change is implemented in the lattice with a series of overlapping local dispersion bumps in the high dispersion regions which reduce the dispersion there. After bunch rotation and adiabatic debunching, which occurs in the first 60 msec of the beam cycle, η will be ramped to .009 to improve stochastic cooling. A ramp from .006 to .009 has already been successfully tested in the Debuncher,[18] although some work is still required on the quadrupole power supply regulation circuits and quadrupole shunt circuits to improve tune control and prevent crossing resonance lines during a fast ramp. This ramp does not change the beta functions anywhere in the ring by more than 5%.

The current momentum aperture of the AP-2 left bend is at least 4%. The limitation is the dispersion in the left bend, where the beam is scraped from nominally $\Delta p/p=10\%$ to

$\Delta p/p$=4%. The question of whether the AP-2 beam line will need to be modified to accommodate a 17% larger momentum spread needs to be investigated experimentally.

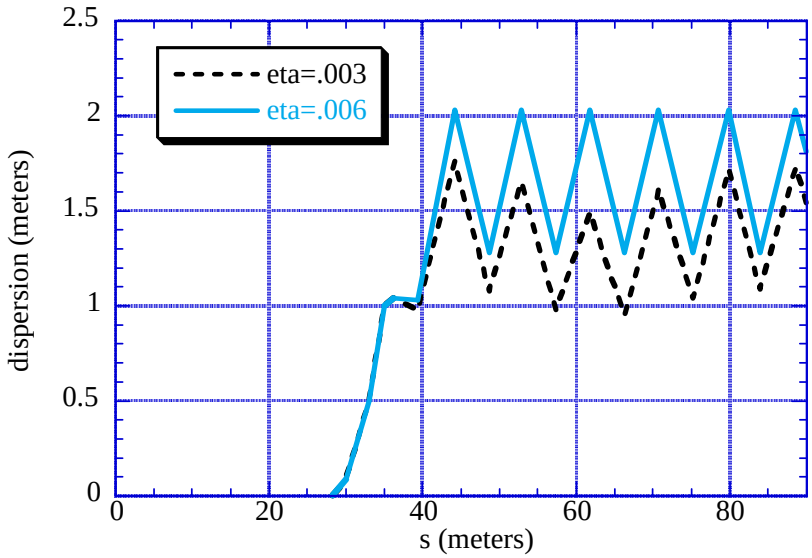

Figure 16. Dispersion function in the Debuncher for 2 different values of η; the 17% increase in momentum aperture comes from the ratio of the maximum dispersion for the η=.003 lattice and the η=.006 lattice.

3.4 Antiproton Bunch Rotation

Bunch rotation is a crucial emittance preservation technique that is used in the production of antiprotons.[19] The effectiveness of the bunch rotation depends on the longitudinal proton emittance in the Main Injector. The process has been simulated using the existing 5 MV rf system and an initial antiproton momentum spread of ±2.4%. The final momentum spread of the antiprotons versus the initial proton longitudinal emittance is shown in Figure 17. For larger longitudinal emittances the Debuncher momentum spread depends linearly on the initial time spread in the proton beam. For very small emittance, non-linearities in the bunch rotation process are responsible for the final momentum spread. In this case, the momentum spread can be reduced by using a higher harmonic rf system in the Debuncher. Figure 17 also shows the momentum spread of the Debuncher beam measured in Run Ib and the bunch lengths expected in the Main Injector for longitudinal emittances of 0.15 eV-sec (nominal Main Injector emittance) and 0.5 eV-sec (slip stacking goal).

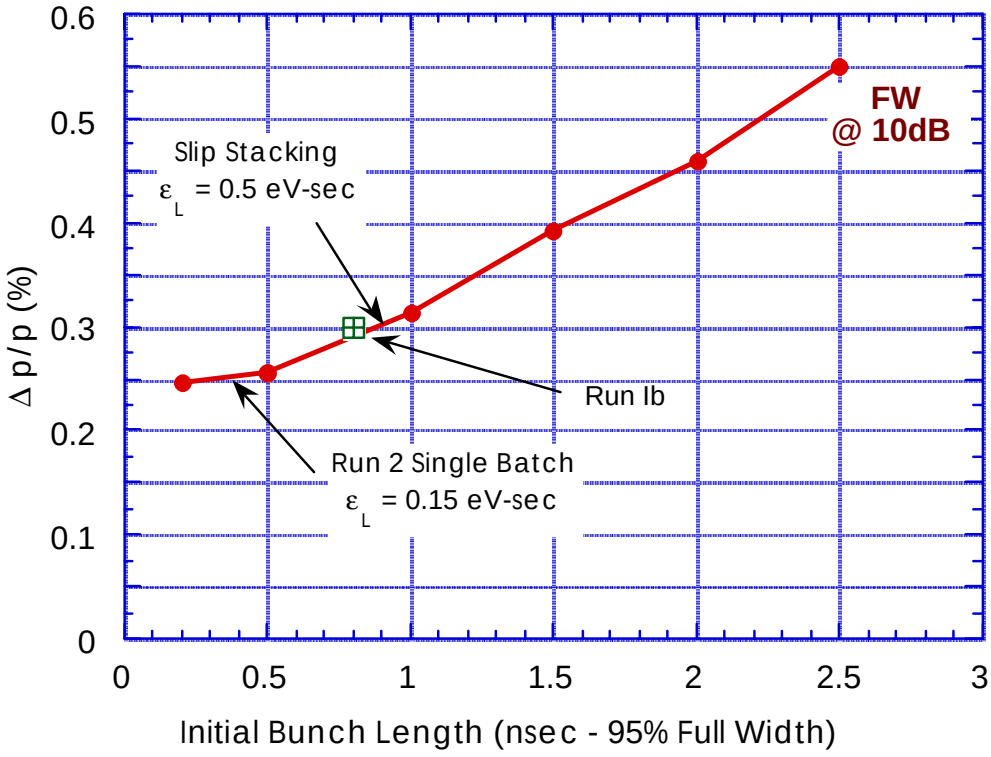

Figure 17. The Debuncher momentum spread after bunch rotation versus the initial bunch length. The width is determined from the full width of the Schottky signal measured at 10 dB down from the peak (FW@10 dB). The Run Ib operating point (measured) is shown as well as a calculated curve.

3.5 Antiproton Cooling Overview

For Run II, an upgrade of the existing 2-4 GHz cooling system in the Debuncher and an upgrade of the 1-2 GHz stack tail cooling system to a 2-4 GHz cooling system will support stacking rates of $2x10^{11}$/hour for Run II. . We plan to use stochastic cooling in the Recycler initially as described in the Recycler Design Handbook (see ref. 3).

An additional factor of 4 increase in antiproton flux can be accommodated by additional upgrades in the Debuncher and the Accumulator to 4-8 GHz. The Debuncher systems would achieve the factor of 4 increase in cooling rate by doubling the bandwidth (a factor of 2) and by reducing the mixing factor (the second factor of 2). The stack tail system in the Accumulator would benefit from an increased bandwidth (a factor of 2), but would have half its cooling load assumed by the Recycler Ring. An important ingredient of this effort is an R&D effort to produce high sensitivity 4-8 GHz pickups and kickers.

In the Recycler an electron cooling system will be used to longitudinally stack the antiprotons for TeV33. Electron cooling promises much higher cooling rates than would be possible with the multi-GHz stochastic cooling systems used in the Debuncher and Accumulator rings. Stochastic cooling rates are inversely proportional to the number of particles being cooled while electron cooling is independent of the number of particles to be cooled. The high beam

intensities in the Recycler favor electron cooling by a wide margin. The rf manipulations and beam transfers are not described in this report but are essentially identical to those described in the Recycler Design Report (see ref. 3) and the Tevatron I Design Report (see Ref. 19).

The cooling calculations assume that 6×10^8 antiprotons are delivered at 2 sec intervals to the Debuncher in 1 nsec bunches with a full (100%) momentum $\Delta p/p=4.8\%$ and a transverse emittance (100%) in each plane of $\varepsilon=32\ \pi$ mm-mrad. The beam is debunched to a momentum spread of 0.3% and cooled to 0.2%. The beam is cooled by about a factor of 4 transversely to 6 π mm-mrad (95%). Table VI summarizes the beam parameters in the Debuncher.

Table VI. Summary of Beam Parameters for Debuncher Cooling

Injected Beam Parameters		
Intensity	6.0×10^8	
Bunched Momentum Spread (full)	4.8	%
Debunched Momentum Spread (full)	0.3	%
Transverse Emittance (100%)	32	π mm-mrad
Extracted Beam Parameters		
Intensity	5.8×10^8	
Momentum Spread	0.2	%
Transverse Emittance (95%)	6	π mm-mrad
Injection Repetition Period	2	sec
Extraction Repetition Period	2	sec

The beam is transferred to the accumulator ring where it is stacked longitudinally and cooled transversely by a factor of 7. Every 60 sec the most dense 8 eV-sec of longitudinal phase space is transferred to the Recycler. The frequency of transfers and the size of the longitudinal emittance depend on the performance of the cooling systems in the Recycler and the Accumulator, and will probably be adjusted in the future. The Accumulator beam parameters are shown in Table VII.

Table VII. Summary of Beam Parameters for Accumulator Cooling

Injected Beam Parameters		
Intensity	5.6×10^{8}	
Momentum spread	0.2	%
Transverse emittance (100%)	7	π mm-mrad
Extracted Beam Parameters		
Intensity	1.6×10^{10}	
Momentum spread	0.06	%
Longitudinal emittance	8	eV-sec
Transverse emittance	1	π mm-mrad
Injection repetition period	2	sec
Extraction repetition period	60	sec

The beam is stacked longitudinally in the Recycler with electron cooling. The nominal stacking cycle is 60 sec, but this time can be varied according to the strength of the electron cooling and the ability of the Accumulator to store beam. The projected Recycler beam emittance shown in Table VII are upper limits, but are anyway smaller than the parameters required for the Tevatron beam parameters (Table II). The smaller emittance, if preserved to low beta, will produce a higher luminosity than those shown in the table. On the other hand, the emittance could be intentionally diluted to avoid instabilities if necessary.

Table VIII. Summary of Beam Parameters for Recycler Cooling

Injected Beam Parameters		
Intensity	1.6×10^{10}	
Longitudinal emittance	8	eV-sec
Transverse emittance (100%)	1	π mm-mrad
Extracted Beam Parameters		
Intensity/bunch	27×10^{10}	
Longitudinal emittance/bunch	<0.5	eV-sec
Transverse emittance	<1	π mm-mrad
Injection repetition period	60	sec
Extraction repetition period	$\sim4.0\times10^{4}$	sec

3.6 Transverse Cooling in the Debuncher

The beam is cooled transversely in the Debuncher by a conventional stochastic cooling system. The process has been simulated by a computer program that is similar to the one used to design the present Debuncher cooling system. This computer program comprehensively describes the stochastic cooling process by solving a Fokker-Planck equation for the beam

distribution as a function of betatron amplitude. The solution includes the effects of good and bad mixing, thermal noise, and signal suppression. The initial and final beam distribution functions are shown in Figure 18. Figure 18 also illustrates the distribution that would be obtained with half the cooling power.

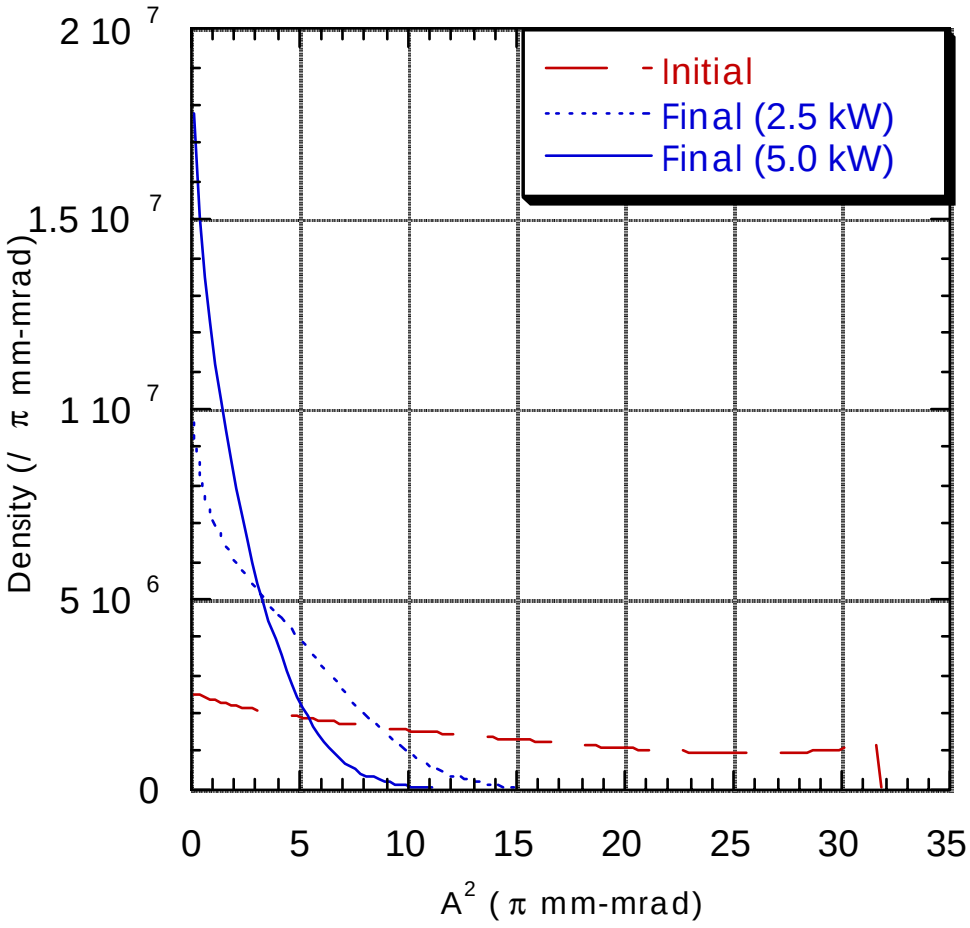

Figure 18. Debuncher transverse cooling simulation.

Since broad band microwave power is expensive, it is important that the power level be kept as low as possible. One of the largest uncertainties in the determination of the required power level is the coupling of the kicker power to the beam. For the purposes of the calculation, a model of an array of strip-line pickups and kickers has been used. The structure actually used will be determined by the 4-8 GHz pickup and kicker R&D program that is described in 3.9.1. It has been assumed that the pickups and kickers are of the "plunging" type and that the aperture is continuously adjusted to maximize the cooling rate while minimizing the loss of particles from scraping on the pickups and kickers. If the impedance is sufficiently high, it may not be

necessary to utilize plunging pickups. The parameters of the beam and the cooling system are given in Table IX.

Table IX. Debuncher Transverse Cooling Parameters.

Number of particles	6×10^8	
Efficiency	93	%
Cycle time	2	sec
Initial emittance	32	π mm-mrad
Final emittance (95%)	6	π mm-mrad
Frequency Band	4-8	GHz
Number of PU's	128	
PU impedance	50	Ω
PU sensitivity	0.8	
PU noise temperature	20	°K
Amplifier noise temperature	40	°K
Electronic gain	145	dB
PU loss factor	0.70-0.77	
Number of Kickers	128	
Kicker impedance	50	Ω
Kicker sensitivity	0.8	
Kicker loss factor	0.65-0.75	
Thermal noise power	1.1	kW
Schottky noise power	3.9	kW
Total power	5.0	kW

The cooling system described above provides about 12× the cooling rate as the system described in the Tevatron I Project Design Report. The major reasons for the improved capability are given in Table X.

Table X. Comparison of the Tevatron I Project and the Proposed Design

Item	Tev I	Tev33	Improvement
Bandwidth	2-4	4-8	2
$\eta = 1/\gamma_t^2 - 1/\gamma^2$	.006	.009	1.5
Mixing	10	5	2
Power (W)	1000	5000	2
Total			12

3.7 Debuncher Momentum Cooling

The Debuncher momentum cooling will be similarly improved by using the 4-8 GHz band. The momentum cooling uses the same pickups and kickers that will be installed for the transverse cooling system. It only requires additional electronics: low noise amplifiers, medium level electronics including a notch filter, and additional traveling-wave tube (TWT) power amplifiers. None of these components present additional challenges beyond those described in the section on Debuncher Transverse Cooling. The performance requirements for momentum cooling are lower (cooling by less than a factor of 2) and the signal to noise ratio is better because the longitudinal signal is stronger than the transverse signal and because the momentum system uses pickups from both the horizontal and vertical systems.

The performance of the upgraded simulation is illustrated in Figure 19. The cooling system parameters used in the simulation are given in Table XI.

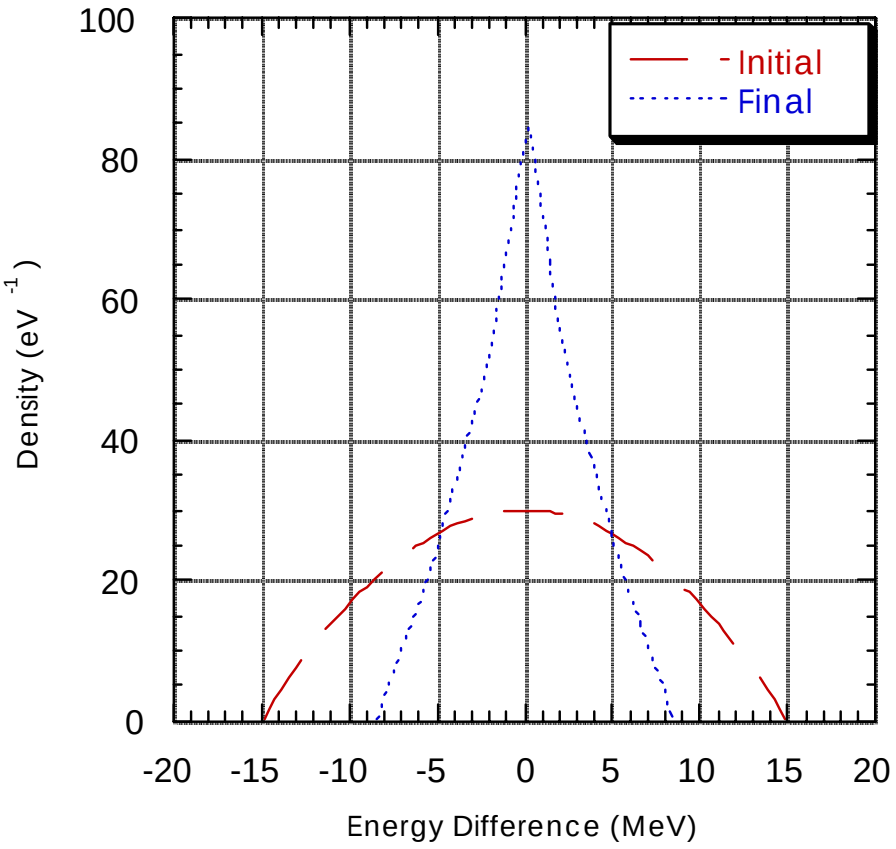

Figure 19. Simulation of momentum cooling in the Debuncher.

Table XI. Debuncher Momentum Cooling Parameters.

Number of particles	6×10^8	
Efficiency	100	%
Cycle time	2	sec
Initial Momentum Spread (full)	30	MeV
Final Momentum Spread (full)	11	MeV
Frequency Band	4-8	GHz
Number of PU's	256	
PU impedance	50	Ω
PU sensitivity	0.7	
PU noise temperature	20	°K
Amplifier noise temperature	40	°K
Electronic gain	140	dB
Number of Kickers	256	
Kicker impedance	50	Ω
Kicker sensitivity	0.7	
Thermal noise power	110	W
Schottky noise power	370	W
Total power	480	W

3.8 Longitudinal Stacking in the Accumulator

The TeV33 longitudinal stacking system is similar in concept to the current stack tail system. A major design consideration is the amount of cooling done. A model, due to van der Meer,[20] relates the rate of accumulation of flux (Φ) to other system parameters

$$\Phi = -\frac{TW^2|\eta|E_d}{p\Lambda} \qquad [10]$$

where W is the cooling system bandwidth, T is the revolution period of the storage ring, $\eta = 1/\gamma_t^2 - 1/\gamma^2$, p is the nominal beam momentum, Λ is a numerical factor Λ=ln2, and E_d is the logarithmic slope of the density distribution $\Psi(E)$:

$$\frac{1}{E_d} = \frac{1}{\Psi}\left|\frac{d\Psi}{dE}\right|. \qquad [11]$$

With the other parameters fixed, an arbitrarily large antiproton flux can be accommodated in the accumulator by tailoring the logarithmic slope of the gain to arbitrarily small values. The consequence of large values of E_d is that less cooling is done in the Accumulator. The cooling deficit (compared to the Run I and Run II designs) will be absorbed by the electron cooling system that will be available in the Recycler as discussed in section 3.10.

The system contains pickups in the high dispersion regions of the Accumulator, correlator notch filters, and kickers in zero dispersion region. The stacking process has been simulated by a computer program that is similar to the one used to design the Debuncher momentum cooling system and the Stack Tail momentum cooling system in the Accumulator. A tutorial description of this process was given in the Tevatron Project I Design Report (see Ref. 19). The computer program comprehensively describes the stochastic stacking process by solving a Fokker-Planck equation for the distribution function. A block diagram of the system is shown in Figure 20.

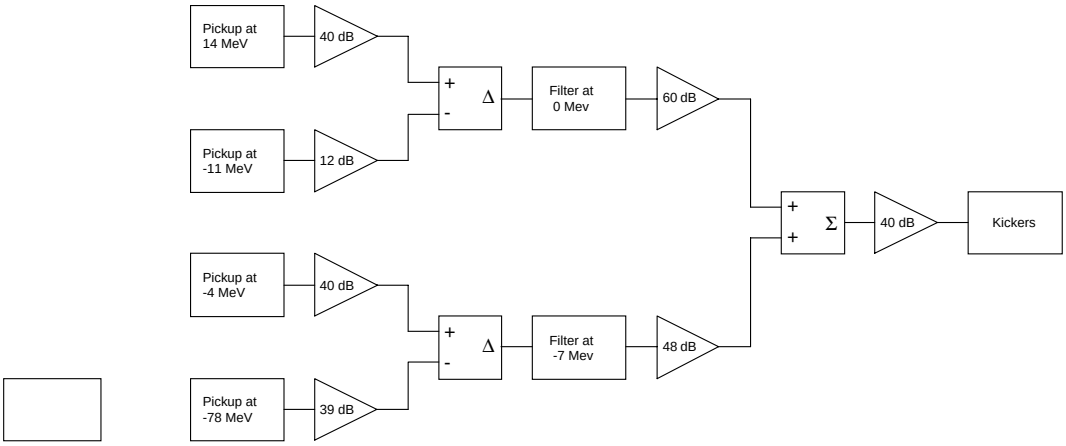

Figure 20. Block diagram of the TeV33 stack tail cooling system.

It is planned that beam would be stacked in the Accumulator for 60 sec. After this interval, the beam would be extracted and transferred to the Recycler Ring. Figure 21 shows the antiproton energy density function at 0 sec (immediately following a transfer to the Recycler) and after 20 and 40 seconds of stacking. The parameters of the beam and the cooling system are given in Table XII.

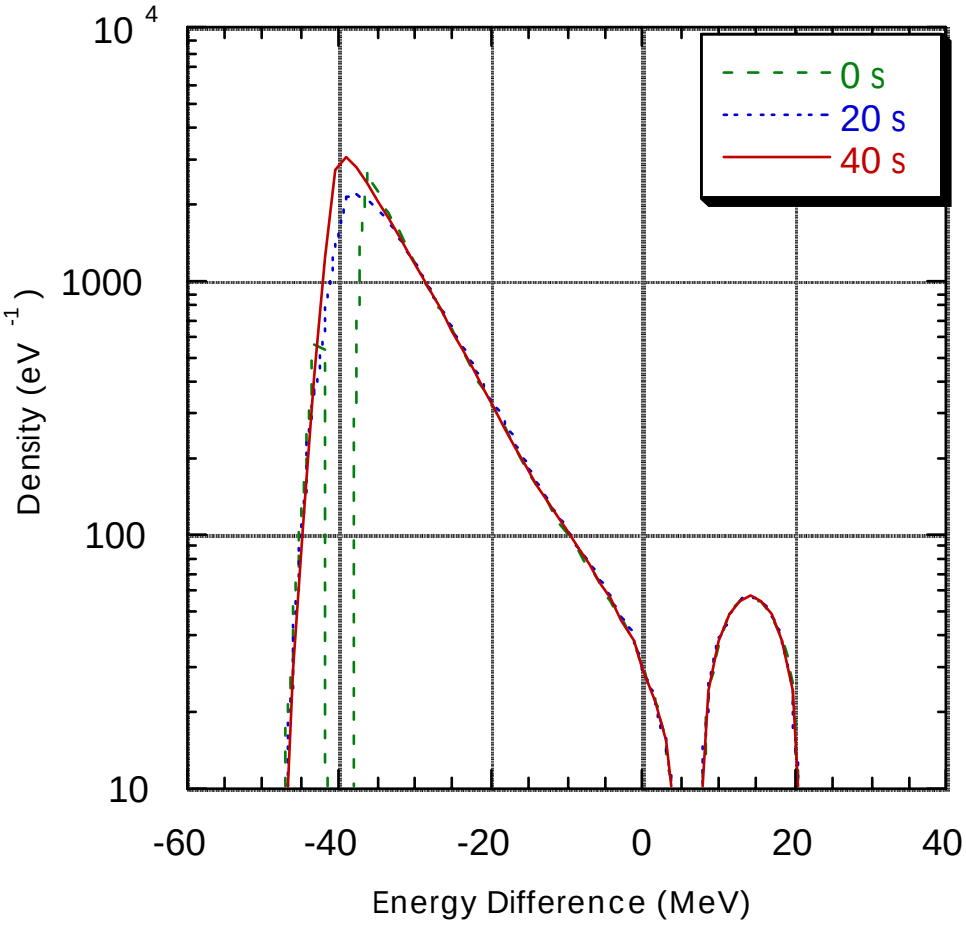

Figure 21. Simulation of Accumulator Stacking. The beam energy distribution $\Psi(E)$ is shown at three equally spaced times during the accumulation cycle. The beam is transferred to the Accumulator just before 0 sec in the cycle creating the gap in the distribution near -40 MeV. The gap gradually fills during the cycle as illustrated by the profiles at 20 and 40 sec.

Table XII. The Accumulator Stochastic Stacking System Parameters

Number of particles	5.6×10^8	
Stacking Efficiency	99	%
Cycle time	2	sec
Initial density	57	eV^{-1}
Final density	3200	eV^{-1}
Final ΔE	5	MeV
Frequency Band	4-8	GHz
Number of PU's	128	
PU impedance	50	Ω
PU sensitivity	0.7	
PU noise temperature	40	°K
Amplifier noise temperature	40	°K
Number of Kickers	128	
Kicker impedance	50	Ω
Kicker sensitivity	0.7	
Thermal noise power	150	W
Schottky noise power	1800	W
Total power	1950	W

3.9 Stochastic Cooling Technology

There are two technologies that are crucial to the success of these upgrades. The first technology is the 4-8 GHz pickup and kicker loops. The second technology is signal transmission which we intend to base on a laser modulation/demodulation scheme. Other technologies including microwave components and amplifiers are commercially available for the 4-8 GHz band.

3.9.1 4-8 Ghz Pickups

Present stochastic cooling electrode technology is based on octave bandwidth planar loops. The gain of these falls off quickly at high frequencies. For example, a 100Ω characteristic strip-line loop has a measured sensitivity of 3Ω at 2-4 Ghz. A similar 100Ω loop has a measured sensitivity of 0.75Ω at 4-8 Ghz.

Many of these low sensitivity broad band loops are combined in binary arrays to form a broad band array. There are a number of problems with binary combiner boards. Even at 2-4 Ghz, they may have large insertion losses and microwave modes. Also, microstrip combiner boards require relatively large areas to avoid undesired coupling between circuit elements. These large circuit boards are difficult to cool efficiently and require large vacuum tanks. Although stripline is electrically superior to microstrip it is much more difficult to deal with mechanically

However, 4-8 GHz slots have been measured to be more sensitive than 3-D loops or planar loops. A single waveguide slot has been calculated to have an effective impedance of 37 Ω over a bandwidth of 0.7 GHz at 6 Ghz as shown in Figure 22. The slot couples

electromagnetic energy from the wakefield of the beam into the output waveguides as shown in Figure 23. The energy of a number of slots can be added together constructively if the phase velocity of the wave in the outer waveguides matches the velocity of the beam. A waveguide without any slots has a phase velocity faster than the velocity of light. The slots act to "slow down" the phase wave in the outer waveguides. The number of slots per length will determine the phase velocity of the wave in the outer waveguides. Research has been started to calculate what line density of slots is needed to match phase velocities. This type of structure is commonly known as a slow wave Floquet structure. This structure is also similar in concept to the 8-10 GHz CERN design of the slow wave ridged pickup array used for bunched beam cooling.

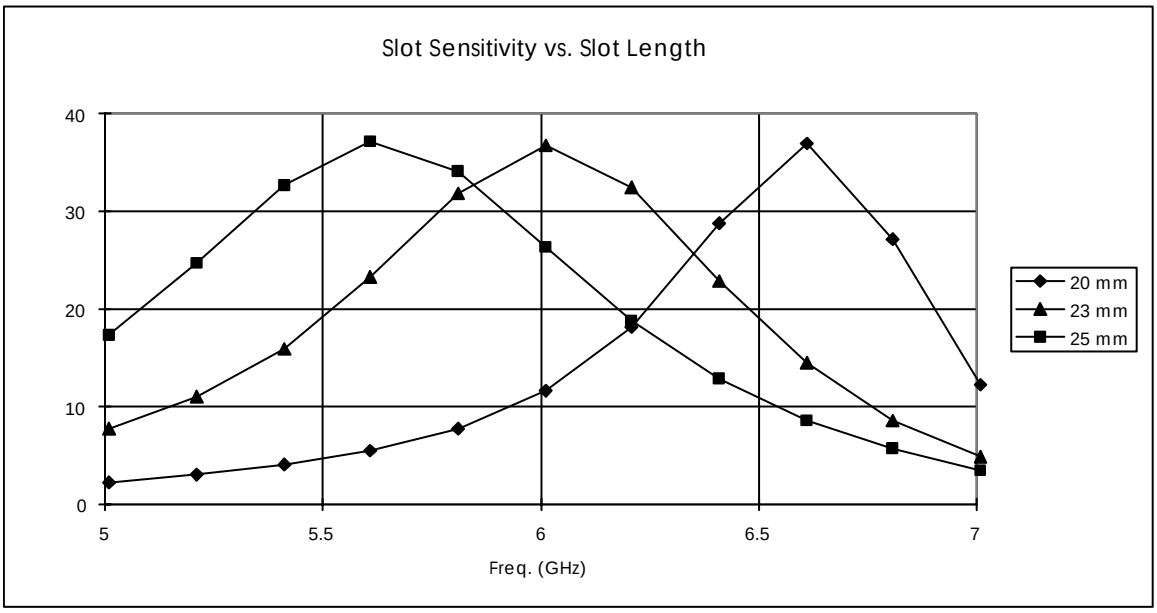

Figure 22. Coupling impedance versus frequency for a single slot of varying width.

Figure 23. A schematic drawing of a 4-8 Ghz slot array.

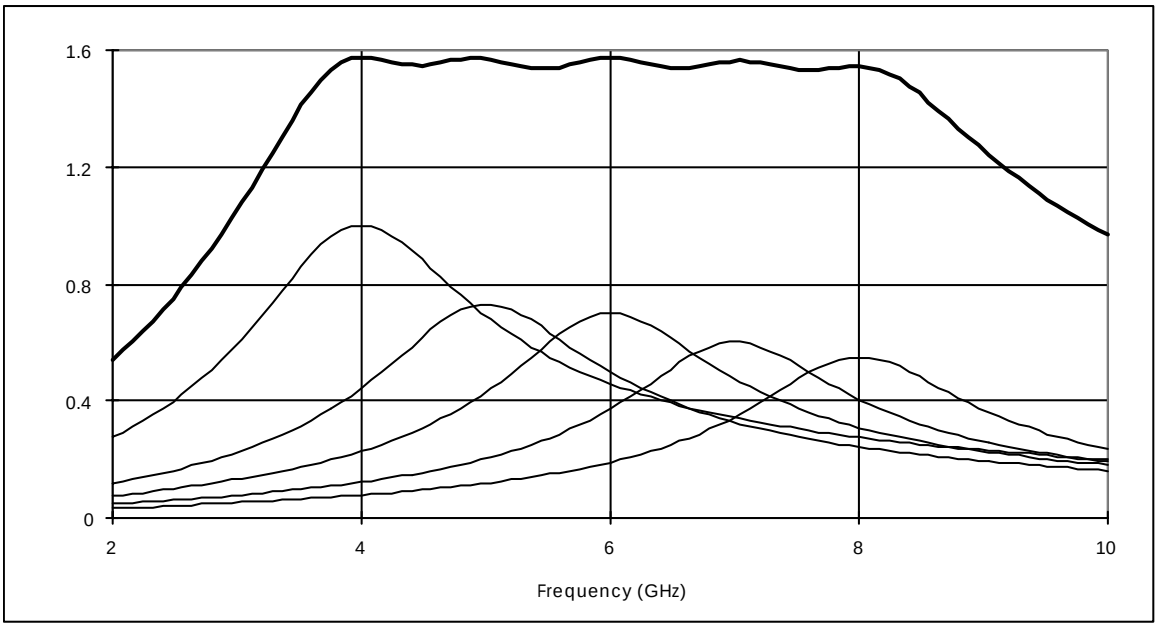

Figure 24. Narrow band arrays are summed to form a broad band response

3.9.2 4-8 GHz Signal Transmission

It is impossible to transmit high frequency microwave signals over long distances with single-mode coaxial cable. As the frequency increases, the cable diameter must decrease to avoid dispersion from higher order modes. At 4 GHz the signal loss in crossing the Accumulator ring is about 40 dB. At 8 GHz it is 80 dB. Light can be transmitted long distances with low attenuation, so a laser modulated at microwave frequencies is an attractive choice for transmitting microwave signals. We already have considerable experience in transmitting signal in optical fibers (for use in microwave notch filters). However, the propagation velocity in optical fibers is too slow to transmit signals across a ring; this transmission must be made in vacuum or air. A disadvantage of using the optical technique is the conversion loss in converting the microwave signal to an optical modulation and the consequent reduction in dynamic range.

Development of an optical microwave link that can propagate a signal in the air has progressed to the bench prototype. Procurement of optical telescopes, beam expanders, and microposition equipment has been completed. The test setup shown in Figure 25 was mounted on a 3 by 6 foot light table. The network analyzer is used in averaging mode. The system is microphonic with ±1 dB of vibration jitter. Some of the important parameters are: the DFB (Distributed FeedBack) laser emits 3.24 mW at 1310 nm, 2.92 mW is transmitted through the second telescope and focused on the second lens/beam collimator. With careful tuning we were able to couple 2.1 mW of this optical power into the single mode fiber. A careful optical/microwave calibration was performed on the system. The microwave calibration was taken at 5 GHz with 16 averages and 3% bandwidth smoothing. The dials on the micropositioner are in microns with one full turn of the coarse adjustments equal to 500 microns. The nanotrak system has piezo motion control of 30 microns in *x* and *y* planes on the micropositioner.

Optical Transmission Test Setup

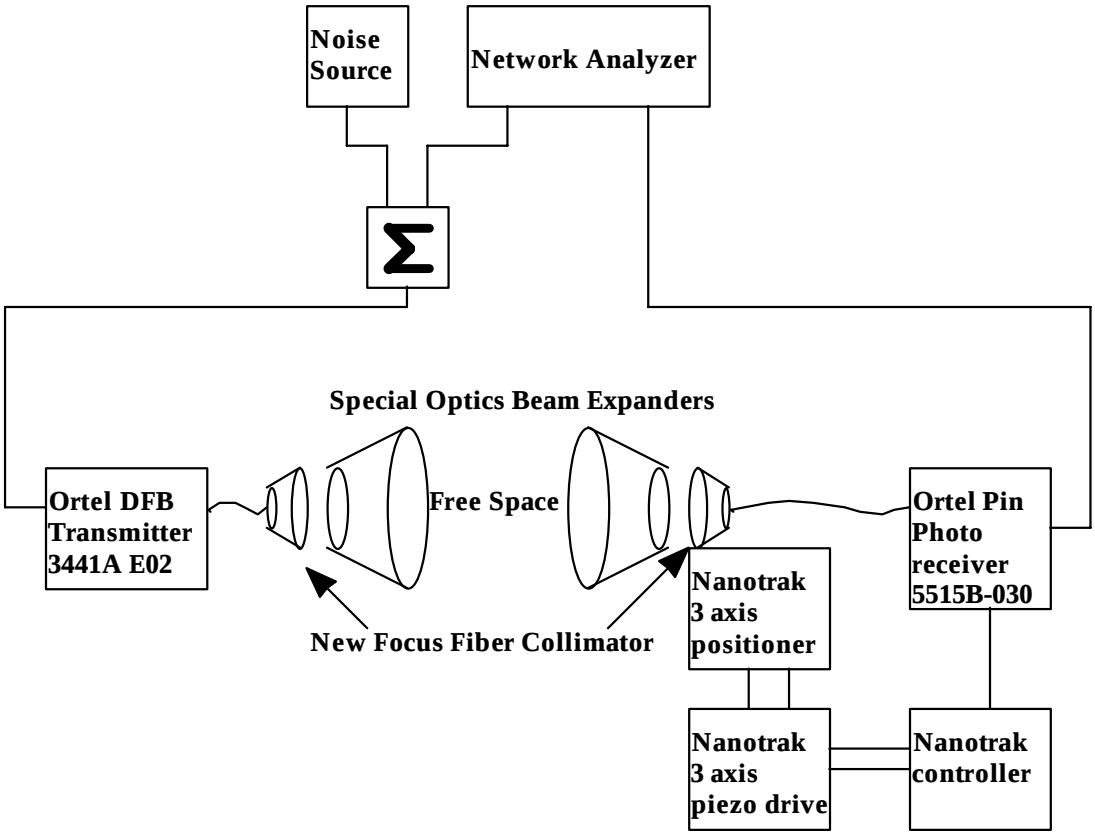

Figure 25. Test set up on 3 x 6 foot light table. Initial results were obtained with 2 inch spacing between beam expanding telescopes.

The transmission (amplitude and phase) obtained with this setup across the 0.5-10.5 GHz band is shown in Figure 26. The stability of the optical link is critical to successful performance of the stochastic cooling. The variations in the optical power and microwave signal with respect to perturbations caused by drifts in alignment, temperature, and other time dependent phenomena are being studied in bench tests. A field test of the optical link will occur this year.

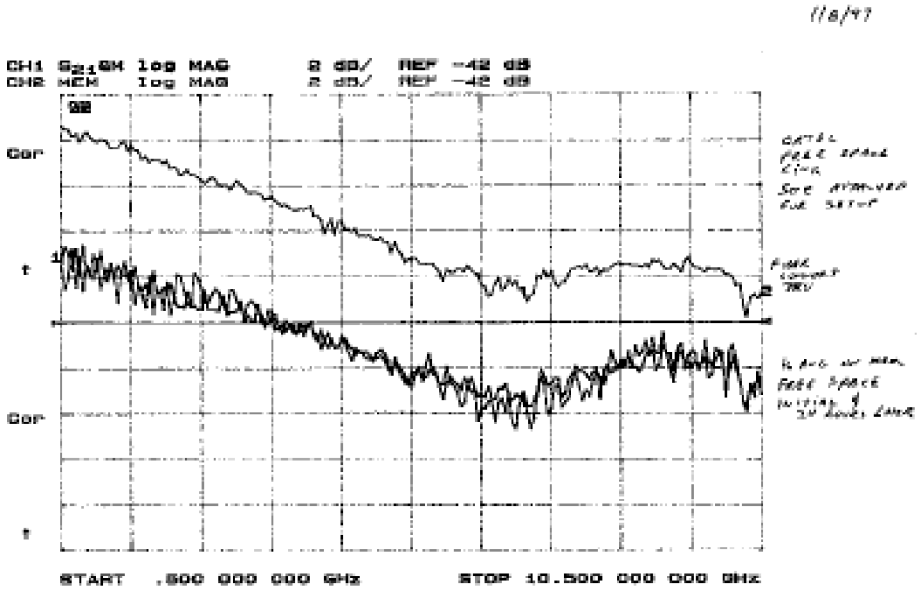

Figure 26. Microwave transmission in the 0.5-10.5 GHz band. The top trace is obtained with a fiber to fiber connect ion. The bottom traces are free space connections obtained over a 24 hour period with position tracking. The vertical scale is 2 dB per division.

3.10 Antiproton Electron Cooling

Electron cooling of the 8 GeV antiprotons in the Recycler provides an attractive solution to the problem of cooling large stacks of antiprotons. The proposed electron cooling system is similar to the one described in the IUCF proposal to cool 12 GeV protons in the SSC Medium Energy Booster.[21] Although electron cooling has now become a routine tool in many laboratories, its use has been restricted to lower energy accelerators (<500 MeV/nucleon). An R&D program is currently underway at Fermilab to extend electron cooling technology to the GeV range.

Since the electron energy has to be approximately 4 MeV, the use of traditional electron cooling technology with a Cockcroft-Walton (C-W) power supply and a magnetically-confined electron beam is impractical. In fact, compact commercial C-W voltage generators are limited to about 1 MV, about a factor of 3 times higher than the IUCF, CELSIUS, and GSI electron cooling systems. In the medium energy regime the Pelletron® (Van de Graaff generator type) electrostatic accelerators, having an operating range of about 2-20 MV, would replace the C-W generators. In this regime the continuous longitudinal magnetic field is no longer strictly necessary for focusing although longitudinal focussing still has advantages. The beam focusing requirements are discussed in more detail below.

®Pelletron is a registered trademark of National Electrostatic Corporation (NEC)

3.10.1 Electron Cooling Rate

Electron cooling is accomplished by merging an antiproton beam with a co-moving electron beam in a short region of a storage ring. Ions moving in the accompanying electron beam rest frame lose energy by Coulomb interactions. The transverse ($1/\tau_{\perp} = 1/\varepsilon_n \, d\varepsilon_n/dt$) and longitudinal ($1/\tau_{||} = 1/\sigma \, d\sigma/dt$) electron cooling times of an ion beam with transverse normalized emittance ε_n and relative momentum spread $\sigma=\Delta p/p$ are well approximated as

$$\tau_{\perp} \approx \frac{A}{Z^2} \frac{\gamma^2}{4\pi\eta\Lambda} \frac{M}{m} \left(\frac{kT_e}{mc^2} \right)^{3/2} \frac{1}{nr_e^2 c} \left[\sqrt{\frac{8}{\pi}} + u_{\perp}^3 \right], \qquad [12]$$

$$\tau_{\parallel} \approx \frac{A}{Z^2} \frac{\gamma^2}{4\pi\eta\Lambda} \frac{M}{m} \left(\frac{kT_e}{mc^2} \right)^{3/2} \frac{u_{\parallel}}{nr_e^2 c} \left[1 + u_{\parallel}^2 \right]. \qquad [13]$$

Eqn. [12] and Eqn. [13] include the effects of the "flattened" electron velocity distribution. A and Z are the ion atomic number and charge state; γ is the usual relativistic parameter; Λ is the Coulomb logarithm (≈10); k is the Boltzmann constant; m and M are the electron and proton masses; c is the speed of light; n is the laboratory frame electron beam density; and r_e the classical electron radius; all other symbols are defined in Table XIII. The quantities $u_{\perp}$ and $u_{//}$ are the dimensionless transverse and longitudinal velocities normalized to the electron beam rms transverse velocity:

[Ed note: Explain flattened]

$$u_{\perp} = \sqrt{\frac{\beta\gamma\varepsilon_n mc^2}{\beta_I kT_e}}; \quad u_{\parallel} = \beta \frac{\Delta p}{p} \sqrt{\frac{mc^2}{kT_e}} \qquad [14]$$

where β is the usual relativistic parameter and β_I is the ion beta-function in the cooling region. Electron cooling is most effective when $u \leq 1$; in this regime the first addends in the square brackets of Eqn. [12] and Eqn. [13] dominate. Note that the longitudinal cooling time (2) is roughly proportional to the ion beam momentum spread. This approximation is only valid for a "flattened" electron velocity distribution and when the longitudinal ion velocity in the moving frame is greater than the electron beam longitudinal rms velocity spread.

3.10.2 Electron Beam Optics

In evaluating Eqn. [12] and Eqn. [13] we have taken the electron beam temperature to be 0.2 eV. This number is somewhat arbitrary but is defined by the following considerations. Let's assume that a standard tungsten dispenser cathode of 7 mm diameter is used, which gives the intrinsic electron beam temperature at the cathode of 0.11 eV, or 1050 ˚C. If we now assume that the electron beam is accelerated and expanded to a diameter of 2 cm, the electron beam temperature becomes 13 meV, or 12 μrad transverse one-dimensional rms angular spread. However, if there exists a misalignment between the electron and antiproton beam trajectories of this order or greater, or if the electron beam optics is not adjusted so as to make the beam parallel to this order or greater, there will be effective temperatures in excess of the cathode temperature.

We feel confident that the two beams can be aligned to better than approximately 40 μrad, and that the angular spread due to the electron beam space charge can be kept below this value, thus giving us a conservative estimate for the electron beam temperature of 0.2 eV. This is not a trivial goal when one considers that the earth's magnetic field alone would cause an electron beam deflection of hundreds of mrad over the 66 m cooling length.

The electron beam is generated in the 4.3 MV terminal of a Pelletron accelerator. Two solenoids at the beginning of the cooling straight produce the required beam size and convergence. Following the cooling straight section, the beam is then transported back to the 4.3 MV terminal and collected. Figure 27 illustrates the layout of the 66 m long cooling section. The simplest electron focusing channel in the cooling region is a series of very weak solenoids with focal length f_{sol} spaced by the distance L_{sol}. Figure 28 shows a typical 2-m long module incorporating the electron beam optics, alignment, vacuum, and diagnostics system in the cooling region. Each solenoid in this module provides just enough focusing to locally correct the electron beam expansion due to its space charge. Consequently, this section is optically equivalent to a drift: to first order, a particle entering off axis, but with no transverse momentum, will leave the section with the same transverse position and with no transverse momentum. Assuming that the electron beam current density is uniform one can obtain a simple relation, connecting the solenoid focal length, f_{sol} , with other parameters:

$$f_{sol} = \frac{r_b^2}{2KL_{sol}}; \quad K = \frac{I_e}{\beta^3 \gamma^3 I_o}, \qquad [15]$$

where $I_0 \approx 17$ kA. Thus, by choosing the 2 m long module, this expression gives the solenoid focal length $f_{sol} \approx 184$ m and the maximum beam divergence in this case is $r_b / (2 f_{sol}) \approx 27$ μrad.

Figure Not Available at This Time

Figure 27. The overall layout of the proposed electron cooling system in the Recycler.

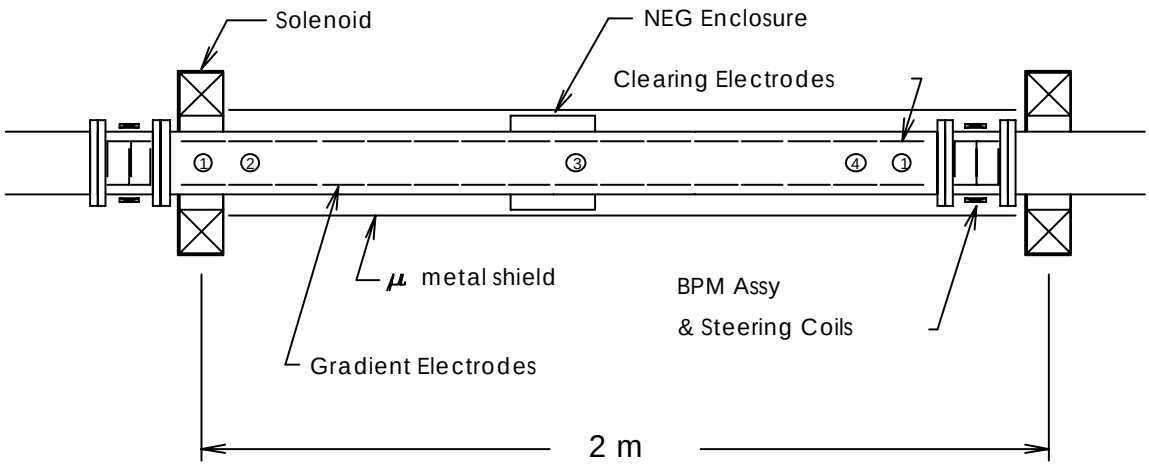

Figure 28. Electron confinement, alignment, vacuum, and clearing system. Every 2 m there is a solenoid, beam position monitor (BPM) and steerer pair, nonevaporable getters (NEG's), and gradient and clearing electrodes.

Such a seemingly simple focusing system is not without drawbacks, however. For example, if the space charge of the electron beam is compensated by a factor of γ^{-2} (≈1%) due to residual gas ions, the electron beam will converge in an uncontrollable way (the solenoids can only focus the beam). In addition, this focusing scheme is susceptible to various electron beam instabilities, which might turn out to be detrimental for the high current electron beam transport through the cooling section. One might also argue that in the case of weak periodic focusing the Coulomb logarithm Λ could be a factor of 2 lower than the value used for evaluation of the cooling times in the previous section. This effect is especially obvious for the "slow" (compared to the time-of-flight through the cooling section) collisions between the electron and antiproton. In this regime the electron is "smeared" by the periodic focusing, thus increasing the minimum impact parameter and, consequently, reducing the Coulomb logarithm. This effect is similar to the reduction of Λ for magnetized cooling. All these phenomena as well as alternate focusing schemes (*e.g.*, a solenoidal field) are currently under investigation.

3.10.3 Technical Considerations

In addition to the electron beam optics design in the cooling region there are two more principal technical problems which need to be addressed in order to build a 4 MeV electron beam cooling system: (1) the electron beam energy regulation and (2) the efficient and stable recirculation of an electron beam. Below, each of these problems is briefly discussed.

3.10.3.1 Electron beam energy regulation

Pelletrons are commercially available with the short-term stability (ripple) of ±20 ppm (parts per million) using a generating voltmeter (GVM) for feedback[22]. This small amount of ripple would have a negligible effect upon the cooling time. Long-term regulation of a Pelletron, however, is substantially worse.[23] Using the standard corona probe feedback system with an

error signal from the GVM, a non-temperature-stabilized Pelletron will drift by as much as 800 ppm/hr, and a thermally-insulated Pelletron by about 75-100 ppm/hr.

Thus, the standard short-term Pelletron regulation should be more than adequate for use in the Recycler. The long-term stability can be greatly enhanced by using an external energy measurement system, for example, a BPM system in a region of high dispersion in the electron beam line.

3.10.3.2 High Collection Efficiencies and Stable Recirculation

Achieving stable recirculation of a nonmagnetically confined electron beam is the most significant technical obstacle. Since a Pelletron accelerator will only source on the order of a few hundred μA, the system must have collection efficiencies of at least 99.99% for operation of a several ampere electron beam. With magnetically-confined beams, such collection efficiencies are easily achieved. In fact, at IUCF, collection efficiencies of 99.9999% have been demonstrated.[24] Our goal is to demonstrate reliable, high efficiency, dc recirculation of a 2 A electron beam using the 2 MV Pelletron accelerator at NEC. Our R&D plan to achieve stable recirculation has been described by Nagaitsev.[25]

Table XIII**.** Electron Cooling Parameters for the Recycler.

Parameter	Symbol	Value	Units
Recycler Ring Properties			
Circumference	C	3319.4	m
Cooling region length	L_C	66	m
Fraction (L_C/C)	η	0.02	
Cooling region beta-function	β_I	200	m
Antiproton Beam Properties			
Momentum	p	8.9	GeV/c
Transverse emittance (rms, normalized)	ε_n		
stacking		1.6	π mm mrad
recycling		3.3	π mm mrad
Momentum spread (rms)	$\Delta p/p$		
stacking		2×10^{-4}	
recycling		9×10^{-4}	
Max. antiproton current	I_p	200	mA
Laslett tune shift	ΔQ_{SQ}	0.01	
Electron Cooling System Parameters			
Electron current	I_e	2	A
Electron kinetic energy	U	4.3	MeV
Electron beam radius	r_b	1	cm
Electron beam temperature	kT_e	0.2	eV
Transverse cooling time (stacking)	$\tau_\perp$	90	s
Longitudinal cooling time (stacking)	$\tau_{//}$	20	s

3.10.4 Alternative approaches

Much of the R&D has concentrated on the Pelletron approach to electron cooling. However, a number of alternatives are also being explored. Many potential alternatives offer substantial cost advantages of the Pelletron. However, it is premature to speculate which if any of these alternatives will be feasible.

3.11 Transfers Between the Accumulator and Recycler

The current plan for Run II calls for the beam to be transferred from the Accumulator to the Recycler through the existing AP3-AP1 line, a remnant of the Main Ring (from F14 to F0), through the Main Injector to the Recycler. In order to accomplish this operation, the AP1 line, which also delivers Main Injector protons to the antiproton target, must be changed from its nominal 120 GeV energy to 8 GeV. It has proven difficult and time consuming in past collider runs to change between 8 and 120 GeV operation in AP1. Even if the tuning problem could be overcome, it would still be necessary to interrupt stacking for a sufficient period of time to change the magnetic fields and establish the timing signals to accomplish the transfer. Å simpler

and probably more effective solution is the construction of a dedicated transfer line between the Accumulator and the Recycler. This new line, known as the AP-5 line, would also have operational benefits for Run II. It is proposed to construct such a line as soon as practical in Run II.

4. Colliding beams issues

4.1 Tevatron Injection

The bunches in TeV33 will probably be spaced at 7 rf bucket (39.5 m) intervals. The trigger electronics for the two major detectors (CDF and D0) are being upgraded for a 7 rf bucket spacing. Smaller spacing between bunches or even unbunched beams have been discussed but are not considered here. A gap in the beam to accommodate injection and extraction (the beam abort) is required.

At the termination of a normal store, only the protons are removed, and they will probably be removed without the use of the abort kickers. However, we plan to use the abort kickers in abnormal situations to remove the beams quickly without quenching the superconducting magnets. The existing beam abort kickers require a minimum gap of 2.6 μsec (139 rf buckets) to rise to a field which is adequate to steer the beam onto the abort dump. The major experimental areas are located at B0 and D0: 1/3 of the circumference of the ring apart. Loading the ring in a three-fold symmetric fashion provides an identical pattern of interactions at the two interaction regions. Non-symmetric patterns are possible and can have some advantages; a non-symmetric pattern would almost certainly be used if there were only one detector.

The antiproton injection kicker has been built for use in Run II and has a rise time of 400 nsec (21 rf buckets). We plan to modify the proton injection kicker to have a similar rise time. The rise times of the injection kickers requires additional gaps in the bunch trains. The bunch loading scheme used in the present analysis, which satisfies the above constraints, calls for three groups of bunches, each 371 rf buckets long to fill the 1113 Tevatron rf buckets. A group consists of 3 batches of 10 bunches spaced at 7 rf bucket intervals. The batches are separated by 20 rf buckets for the injection kicker and the last batch is followed by the abort gap of 139 empty buckets. This scheme is illustrated in Figure 29

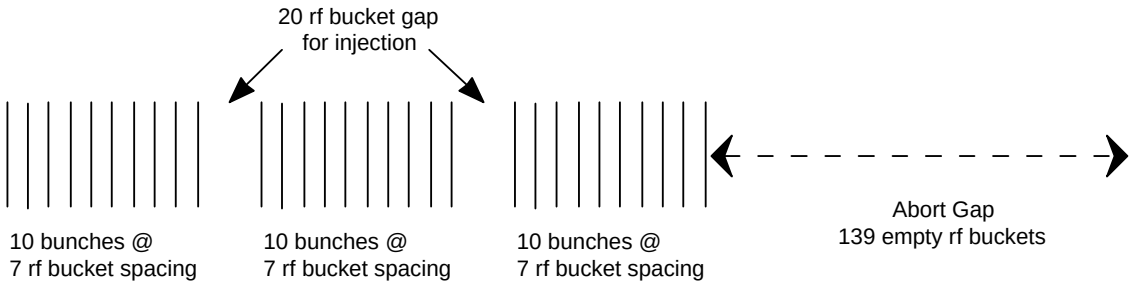

Figure 29. Nominal bunch structure for TeV33.

The gaps in the beam cause an undesirable spread in the beam-beam tune shift parameters. With the scheme illustrated in Figure 29, only 90 out of 159 potential rf buckets are filled. If some of the gaps were eliminated or reduced, and the total number of antiprotons were held constant, the number of interactions per beam crossing could be reduced. We expect that the actual configuration of bunches will change as we study the beam-beam interaction and the beam loading constraints in more detail.

4.2 Proton Intensity

The TeV33 proton intensities are specified to be the same as those used in Run II and, in fact, already achieved in the Main Ring. Simulations predict that 5 bunches, each with $6x10^{10}$ particles in a longitudinal emittance of 0.15 eV-sec can be coalesced into a single 1.38 eV-sec bunch with $30x10^{10}$ particles.[26]

A simulation for seven bucket spacing has also been performed. In order to achieve good coalescing efficiency with 5 bunches, the rf wave-form must be linearized using higher harmonics of the rf. The simulation used first, second, and third harmonics of the basic 7.58 MHz frequency (7 bucket spacing). The results of the simulation are shown in Figure 30. Each of these frequencies would be created by a new, albeit modest rf system. The new rf systems are summarized in Table XIV.

Based on beam experiments with multi-batch coalescing, we know that beam loading effects are important. The simulation has not taken these effects into account. Some of the measures we plan to use to reduce beam-loading effects are discussed in section 3.1.3.3. The number of batches that can be simultaneously coalesced will affect the loading scheme. At the moment, we plan to simultaneously coalesce 10 batches.

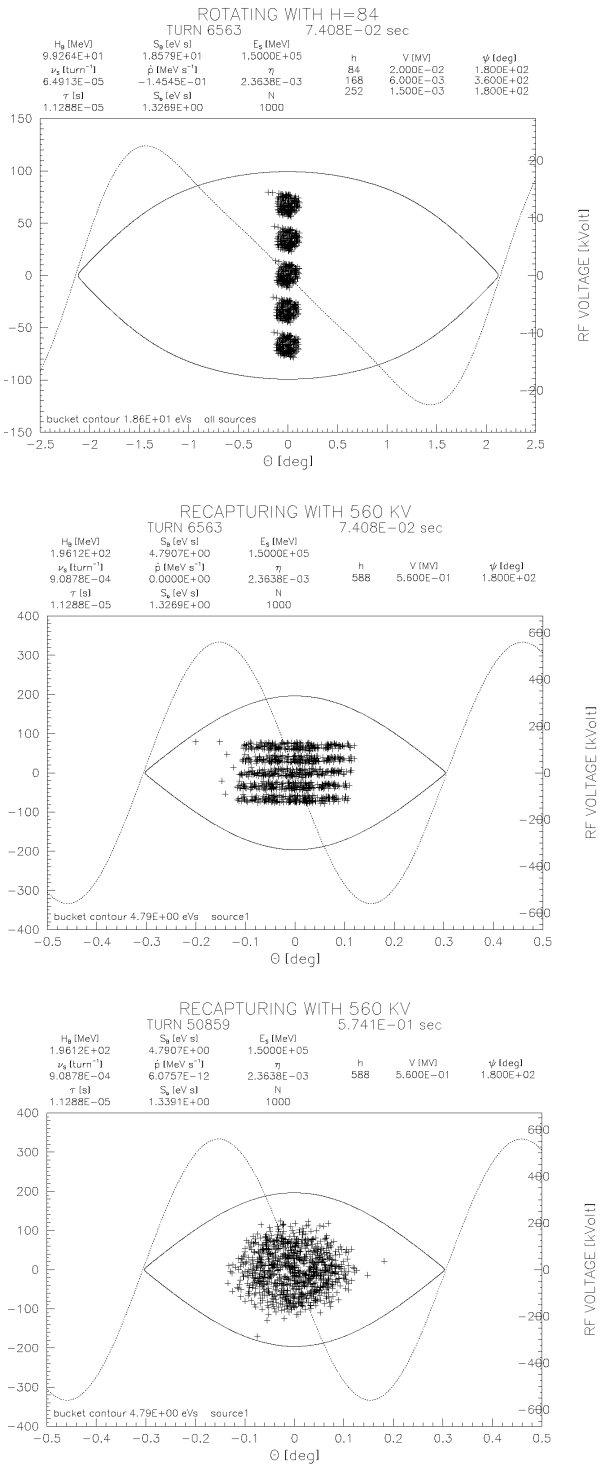

Figure 30. A simulation of the proton coalescing process. The beam distribution and rf wave form is shown (a) after rotation with the (linearized) *h*=84 rf, (b) immediately after recapture with the *h*=588 (53 MHz) rf, and (c) as the beam approaches its equilibrium distribution in the *h*=588 bucket.

Table XIV. New rf systems required for proton coalescing in the Main Injector

Harmonic	Frequency (MHz)	Voltage (kV)
84	7.59	20
168	15.17	6
252	22.76	1.5

4.3 Antiproton Intensity

The proton coalescing hardware could be used to form the antiproton bunches, but it is likely to be unnecessary. The Main Injector is expected to be capable of accelerating 0.5 eV-sec bunches through transition with the 53 MHz rf system. The total Recycler longitudinal beam emittance will be less than 50 eV-sec in stacking mode (see Table XIII). The Recycler beam could thus be packaged into batches of 12 bunches with 7 bucket spacing, each bunch having an emittance of 50/100=0.5 eV-sec or less. These bunch trains could be accelerated directly by the Main Injector provided that collective effects do not cause any serious problem. An alternative approach, that we plan to use in Run II, is to use a lower harmonic rf system in the Main Injector. The Run II plan, for example, calls for the acceleration of 1.5 eV-sec bunches in the Main Injector with the 2.5 MHz (coalescing) rf system and a reduced ramp rate.

In any event, the Recycler, with electron cooling, has the potential to deliver much smaller emittance beams than the 2 eV-sec listed in Table II. Such low emittance bunches could produce large tune shifts in the proton beam, be subject to rapid growth from intrabeam scattering, and be subject to instabilities (such as the fast head-tail mode). We may choose to dilute the beam to the 2 eV-sec emittance listed in Table II in order to avoid some of these effects, or we may choose to take advantage of the increased luminosity available from lower emittance beams. If we should find it necessary to blow up the emittance before transition in the Main Injector, we would use the coalescing technique described in section 4.2 for the protons also.

4.4 Tevatron rf voltage considerations

One of the more important factors in the luminosity form-factor (F in Eqn. [1]) is the bunch length. The bunch length is determined by the rf voltage and the bunch emittance. For gaussian beams in a stationary bucket having emittances small compared to the bucket area:

$$\sigma_\ell = \sqrt{\frac{\eta \varepsilon_L^2}{18\pi (ehV) E_0 \omega_0^2}} \qquad [16]$$

As shown in Table II, the existing 1 MV of rf at 53 MHz results in an rms bunch length of about 36 cm. This can be reduced to 13 cm with a 16 MV system operating at 212 MHz. Figure 31 shows a comparison of the average integrated luminosity that could be obtained with and without the rf upgrade[27].

The evolution of the beam emittances during a store is expected to be dominated by intrabeam scattering and should be rather different in the cases with and without the rf upgrade. The evolutions of longitudinal and transverse emittances are shown in Figure 32 and Figure 33.

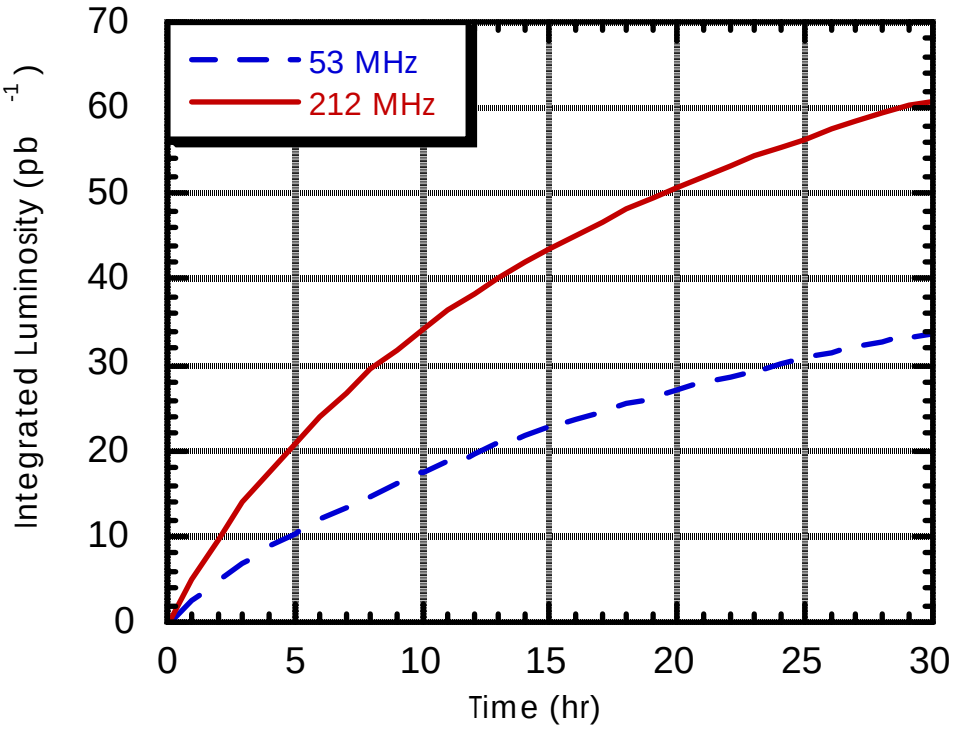

Figure 31. The average store luminosity as a function of time between stores. The average luminosity increases with store length because there is more time to accumulate antiprotons and the initial antiproton intensity is higher.

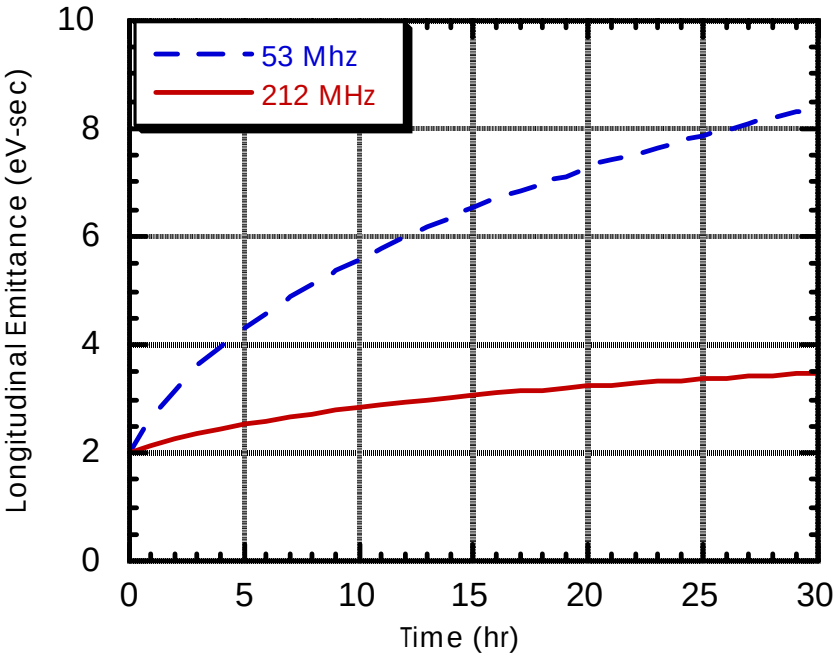

Figure 32. The longitudinal emittance as a function of time into the store. The larger momentum spread obtained with the higher voltage, 212 MHz rf system dramatically reduces the longitudinal growth.

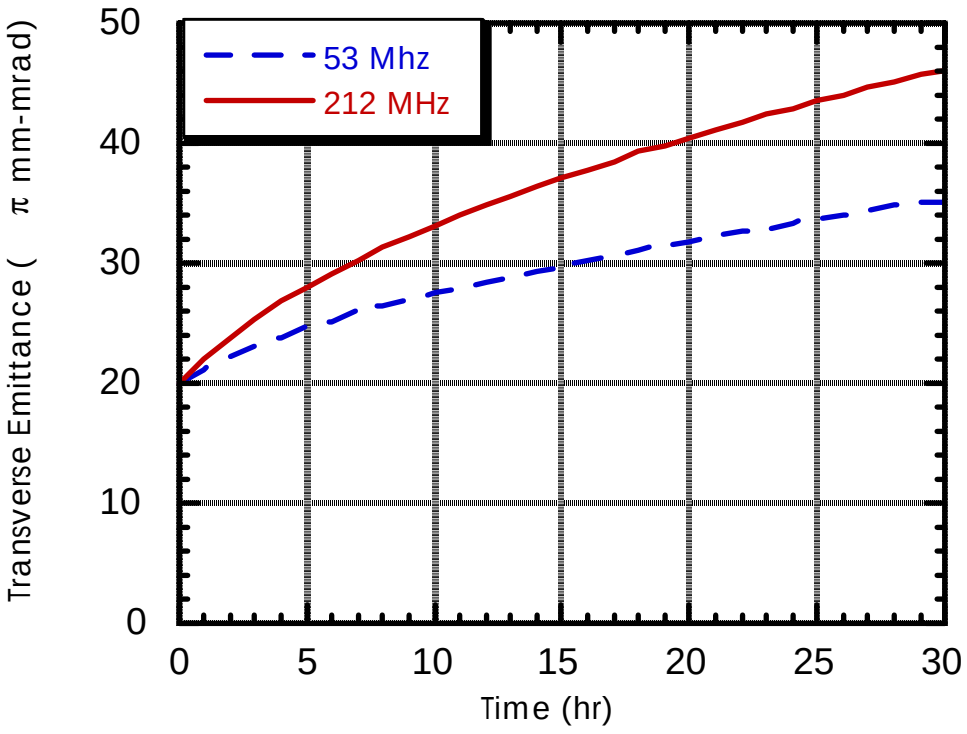

Figure 33. The transverse emittance as a function of time into the store. The shorter bunch length obtained with the 212 MHz rf system increases the transverse beam growth.

Stronger rf focusing could be obtained with either conventional or superconducting technology. Since no power is delivered to the beam when the beams are stored, superconducting technology is a natural choice. With an inductively tuned superconducting cavity, the beam current will excite the cavity, producing the necessary voltage. While this approach appears promising, it will be necessary to establish the techniques required to capture the beam into the desired buckets and to examine the beam stability. We have postponed a more detailed look at these beam dynamics issues because the rf upgrade, if feasible, will be an expensive proposition and will occur, if at all, in the later stages of the TeV33 upgrade.

4.5 Single beam stability

Beam instabilities can be divided into two types: single-bunch and multi-bunch instabilities. The single-bunch may be caused when a bunch's wake fields act on itself. Multi-bunch instabilities may be caused when the wakefield acts on subsequent bunches. The proposed single bunch intensities for TeV33 are essentially the same as those already achieved. Therefore, the instabilities expected are those known from current operation. A head-tail transverse instability is observed[28] when the chromaticity is negative. In normal operation, the

chromaticity is maintained at about ξ=+10 to provide a margin against this instability. When the beams are colliding, where the instability is presumably stabilized by the tune spread from the beam-beam tune shift, the chromaticity is reduced towards zero. The long range beam-beam tune shift in TeV33 results in a spread in bunch-by-bunch chromaticities, so we plan to suppress the instability with the new Tevatron bunch-by-bunch damper. The damper may cause excessive emittance growth if used for more than a few minutes, but we expect beams should be stable when collisions are achieved.

We have also observed what appears to be a longitudinal head-tail instability.[29] This instability is suppressed by a longitudinal bunch-by-bunch damper designed for 6 bunch operation.[30] This damper system will need to be upgraded to handle 36 bunches(21-rf bucket spacing) in Run II and ultimately the 7-rf bucket for TeV33.

Multi-bunch instability thresholds depend primarily on the total current. TeV33 operation will be significantly more susceptible to multi-bunch instabilities than was the case in Run I (6 bunch operation). However, based on fixed target operation (with 2.5×10^{13} particles), we expect transverse instabilities from the resistive wall effect and longitudinal coupled bunch instabilities from the cavity modes. The resistive wall instability is not seen in the Tevatron when the chromaticity is tuned to be positive. The most severe longitudinal coupled bunch instability appears to be a mode-1 instability. Since neither of these instabilities is particularly vicious in fixed target operation, we expect to be able to control them in Collider operation.

4.6 Beam abort

The role of the Tevatron abort will change dramatically when antiproton recycling becomes a reality. The existing A0 abort removes protons and antiprotons from the accelerator simultaneously in a single turn and consequently cannot be used if the antiprotons are to be retained at the end of the store. The role of the A0 abort in Run II and beyond would be to:

1) Provide a beam dump when proton-only stores are used (including the normal tune-up of beam transfers.
2) Remove colliding beams urgently–to avoid a quench, for example.

The effectiveness of the abort for colliding beams is limited by the following factors:

1) It is difficult to develop a signal that reliably indicates the need for an urgent abort. For example, the loss monitor system that is used in fixed target operation is not allowed to trigger the abort in colliding beams operation.
2) Some faults (such as a refrigeration failure) typically result in quenches whether or not the beam is removed.
3) There are times during the injection process and possibly during acceleration when the beams are not appropriately cogged to make possible an abort without excessive (quench inducing) losses.

Despite the limited use of the A0 abort, we tentatively plan to retain it in its current configuration and to use it whenever possible to minimize the number and the severity of quenches and to provide a more controlled removal of the beam energy and better confinement of the resulting radioactivity.

The intensity limitations[31] of the A0 abort are summarized in Table XV. The yearly dose rates assume a utilization of 7200 proton beam aborts at 150 GeV, 6 proton beam aborts at 1 TeV, and 2 antiproton beam aborts per day for 183 days per year. The most serious limitations are the activation of the absorber and soil contamination. The soil contamination problem can be mitigated by the addition of steel on the outside of the existing absorber. The 0.1 rad/hr limit on the residual activity is somewhat arbitrary but could probably be reached by adding some additional shielding to the existing absorber.

Table XV. Intensity limits of the A0 abort

Subject	Limiting Parameter	Max Beam Intensity
Beam loss (quench)	<0.1 mJoule/gm	2.6×10^{14}
Residual Radioactivity	<0.1 rad/hr @ 24 hr	4.4×10^{12} @ 150 GeV
		2.6×10^{12} @ 1 TeV
Energy Deposit. in Graphite	3 KJoule/gm	4.5×10^{13} @ 1 TeV
Hadrons in Soil	<1.5 E16/yr @ 1 TeV	2.2×10^{12} @ 150 GeV
		1.3×10^{12}@ 1 TeV
Thermal Power (average)		Not a problem
Muons flux		Not a problem

4.7 Interaction Regions

It has not yet been decided how many interaction regions will be occupied by experiments during the TeV33 era. One or both of the major interaction regions at B0 and D0 might be occupied. A proposed, new interaction region at C0 might also be occupied. We have not considered in any detail at all, any option other than the current operating condition of having high luminosity experiments at B0 and D0.

The low beta insertion at C0, if any, has not been designed (although there has been a significant effort towards this end). The low beta insertions at B0 and D0 are likely to undergo some modification probably at the time of Run II. These modifications, which are described below, have been used in the calculation of the beam-beam effects.

4.7.1 Lattice

A low beta insertion which is matched to the Tevatron and which yields zero for both η and η' in the IR has been described.[32] This insertion uses the current physical configuration of the IR and the magnets gradients can be achieved with the already installed quadrupoles. Implementation of this design would only require the interchange of two power supplies and a reversing switch. For β^*= 0.35m, the IR lattice functions and the corresponding quad gradients for this dispersion-free solution are shown in Figure 34 and Table XVI. Compared to the Run I optics, this solution results a slightly smaller beam in the IR and also appears to have a beneficial side effect on the beam separation. Just after the separators, in the plane with the most separation, the new insertion has stronger focusing, resulting in a faster betatron phase advance, and a more rapid separation of the beams. But, the lattice has not yet been optimized for the

beam-beam effects. One particular problem we hope to consider in the future in the modification of the horizontal phase advance between the horizontal separators at B11 and B17.

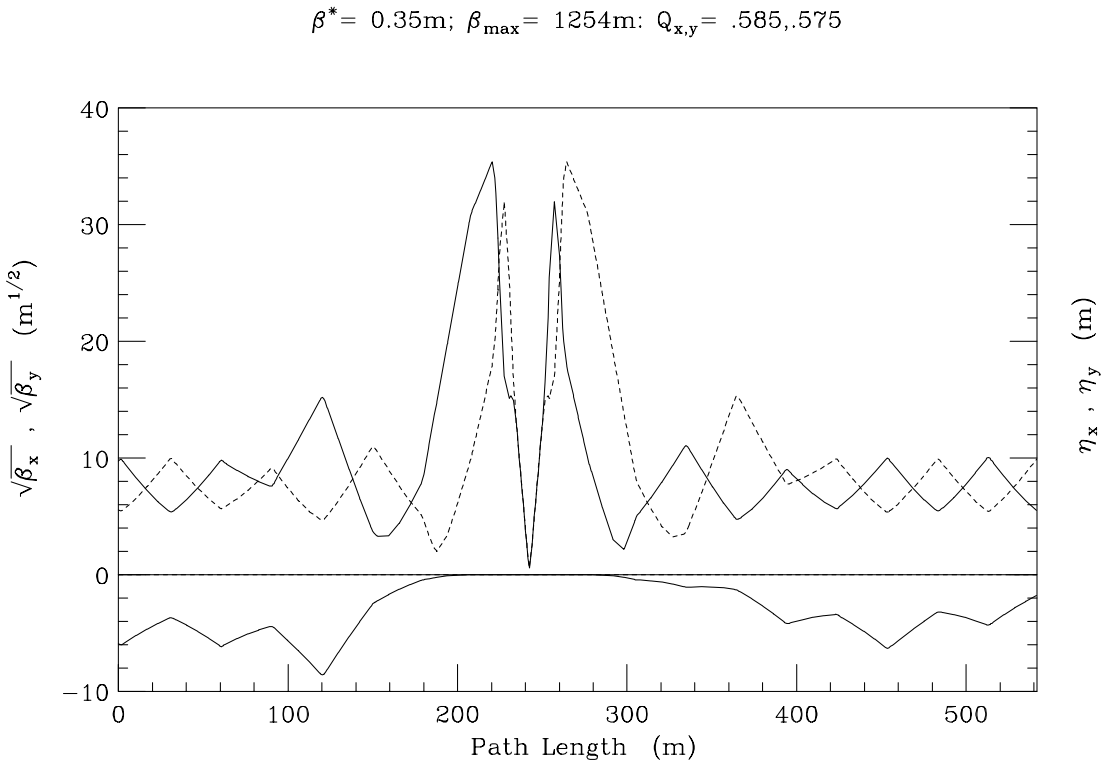

Figure 34. Dispersion-free IR lattice functions for β^* = 0.35m.

Table XVI. IR quad gradients for β*=0.35 m

Quadrupole	Gradient (T/m)	
	upstream	downstream
Q4	120.0349	-120.0349
Q3	-123.9186	123.9186
Q2	120.0349	-120.0349
Q1	31.2039	-31.2039
Q5	-133.0558	133.0558
Q6	-26.6276	26.6276
T6	-1.96143	
T7	33.2027	-32.5509
T9	-46.4417	48.3786
T0	9.08524	-10.7146

4.7.2 Magnitude of the crossing angle

The first parasitic crossing for TeV33 occurs just 19.8 m from the interaction point (IP), placing it within the interaction region (IR) triplet quadrupoles and before the first set of separators. It does not appear possible to avoid collisions at these points without introducing a crossing angle at the IP. A straightforward calculation [5] shows that additional separators inboard of the IR triplet quadrupoles would have little effect on beam separation at the first crossing. Essentially all the betatron phase advance occurs in the immediate vicinity of the IP, and is practically zero across the IR triplet quadrupoles. For realistic gradients and lengths, electrostatic separators are incapable of producing the 3-5σ beam separation desired, with θ=0 at the IP. Without a crossing angle the additional crossing points would more than triple the beam-beam tune shift arising from the interaction point.

Ultimately, the size of the crossing angle will be determined by operational experience. A priori, this choice is not obvious. The crossing angle represents a compromise between avoiding excessive beam-beam effects from the parasitic crossings nearest the interaction point and the reduction in luminosity resulting from a crossing angle. The *half*-crossing angle θ that produces $n\sigma$ beam separation at the first parasitic crossing is approximately:

$$\theta \approx \frac{n}{2} \cdot \sqrt{\frac{\varepsilon}{6\pi\beta^* \beta_r \gamma_r}} \qquad [17]$$

where $\beta_r = v/c \approx 1$. For 3σ and 5σ separations θ becomes approximately 142 and 236 μrad, respectively. We have chosen to divide the crossing angle equally between the horizontal and vertical planes at each IP (θ_x=θ_y=100 and 170 μrad, respectively).

4.7.3 Effect of the crossing angle on the luminosity

Because our bunches are very long (either about 37 cm with the present Tevatron rf system or about 14 cm if we implement the rf upgrade described in section 4.4) with very small transverse beam sizes at the interaction point (about 30. microns), the crossing angles we are contemplating are not small. They have significant effects on the overlap of the beams and so on the luminosity and on the beam-beam tune shifts. Figure 35 shows the form-factor in the luminosity equation as a function of crossing angle for the two bunch lengths assuming the remaining parameters are those given in Table II. The third bunch length (54 cm) can be obtained with a 4 eV-sec beam in a bucket formed by 1 MV at 53 MHz.

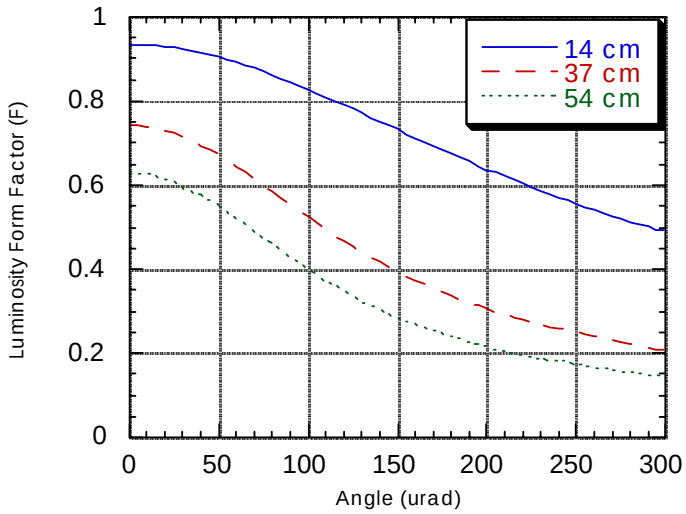

Figure 35. The luminosity form-factor as a function of angle. The angle is the half-angle in either plane: it is assumed to be the same horizontally and vertically.

4.7.4 Effect of the crossing angle on the z distribution

The *z* distribution at the colliding beam can be calculated easily once the bunch length and the crossing angle are known. Figure 36 shows the distribution of vertices for 170 μrad crossing angle assuming various bunch lengths.

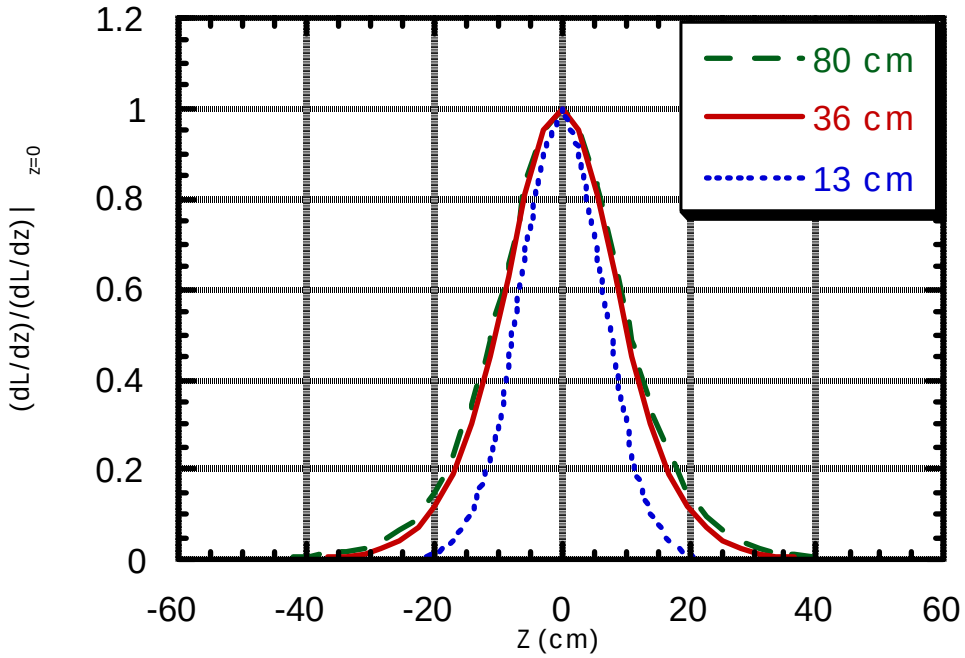

Figure 36. The calculated z distribution of vertices for a 170 μrad crossing half-angle in each plane and various bunch lengths. For bunch lengths of 35 cm or more, the distribution is largely determined by the size of the crossing angle.

4.8 Beam-beam effects

Peter Bagley is working on section 4.8. The current text is just notes for the final version.

Introduction: Importance of the beam-beam effect.

4.8.1 Bunch-by-bunch tune shifts

Give equations. Mention the fundamental variables.
(Assume x0n, y0n, s0n = 0, then xi/xi0 depends on thnx, thny, and sigs/beta*.)
I think we should also explicitly say that the snowmass result for xi vs crossing angle is wrong due to its using a bunch length a factor of 2 too large.

Figures xxx to zzz show the luminosity and the tune shifts and transverse coupling for zero amplitude particles.
These graphs have curves for bunch lengths of 37 cm and 14 cm.

Give the other parameters used for the graph.
At zero angle, the luminosity is a little lower than the simple expression due to the hourglass effect. For a bunch length of 37 cm, half horizontal and vertical crossing angles of 100, 136, and 170 μrad decrease the luminosity by factors of xxx, yyy, and zzz, respectively.
Big hit in luminosity
For a bunch length of 14 cm, half horizontal and vertical crossing angles of 100, 136, and 170 μrad decrease the luminosity by factors of xxx, yyy, and zzz, respectively.
With the shorter bunch length there is a greater overlap of the bunches and less luminosity is lost.

May want a picture of the bunches crossing at an angle. (MacDraft ??)
Comment that the
Because of the large crossing angles, the bunches only overlap near the beta minimum and the hourglass effect is greatly reduced.

This is a good place to put in the bit on the longitudinal distribution of the events.

Include a version of the graph of lum, xi vs crossing angle.
Since we have room I would tend to put in something closer to my version, with curves for35 cm and 14 cm bunch lengths, and showing lum, xi, and xisq.
If we show more than one bunch length, the reference lum should be the head on, short bunch limit, so the difference in the hour glass effect for the 2 bunch lengths can be seen.

4.8.2 Choice of equal horizontal and vertical crossing angles.

Show and explain figures for sum of +-2, +-1, 0 points for
(theta = 140 and 240 urad) and for (bunch lengths of 37 cm and 14 cm).
Adjusting the signs of the crossing angles can change the signs of the coupling components, but does not change the sign of the tune shift components.
By making the crossing angle all horz at one IP and all vert at the other IP, get similar total horz and vert tune shifts. But get smaller total tune shifts if use about equal horz and vert crossing angles at both IP's.
Give numbers for these cases.
Tune shift components never get very negative, can't get very much cancellation.
With two IP's we can chose signs that make the xisqcos largely cancel.

4.8.3 Choosing our favorite combinations

Introduce idea that there isn't much room in the lattice for more separators and very little flexiblity as to where they could be put. 11 and 49 locations are already filled with separators. 48 and some 17 locations available as well as some space near some 0 locations.
Put in sketch of dipoles and orbit ?

To keep machine closed, the bend center can not move. If you move a "space", have to split it. End effects are expensive (need bypass boxes for helium and bus work)
Move by one dipole, dr is 5.0 cm
Move by one cell (e.g. A22 to A23) dr is 24 cm
Move by one house (e.g. A22 to A32) dr is 1.9 m.
Can't move "spaces" very far.
Separators must be at efficient locations (High beta in kick plane.)

Main problems are from first few crossings near the IP's
Separations and behavior of these first few crossings are entirely determined by the optics, the settings of 49 and 11 separators, and the signs and sizes of the crossing angles at the IP.
Have many possible combinations of signs of crossing angles and size and signs
of the pieces of the helix.
However not every combination is allowed at the 2 IP's. The helices in the arcs must match together.
Discuss procedure for choosing favorite combinations.
2 series -- For jj15c and a given size of the crossing angles, chose a fairly large helix in the arcs, then ran through all 32 combinations of the signs of the pieces of the helix and the signs of the crossing angles. Main considerations were the min. diag sig sep, the no. of points with dss <4, the min ((diag sep)/(sigma max)).
3 and 4 series -- For jj15c and a given size of the crossing angles, looked at the combinations of sizes of the 11, 49 location separator kicks and the signs on the crossing angles and the sep kicks that would give the best results. Again main considerations were the min. diag sig sep, the no. of points with dss <4, the min ((diag sep)/(sigma max)).
(Don't show the gen tables, but try to give an idea of what they represent.)
Example configurations shown in this figure are an attempt at producing good behavior at these first few near misses. Don't worry too much about separator settings being reasonable.
We are beginning to believe that the 100 urad case (corresponding to 3 sigma center to center separations at the first 2 crossings) is too small of a crossing angle. So we have not made 3 and 4 series versions for the 100 urad configuration. Despite this, we have not entirely ruled out the 100 urad case.

Present basic parameter set.
Describe and give equations for zero amp calculations.

pppp2.100npnn
pnpp3css.136nppp
pnpp4ass.170nppp

4.8.4 subsection -- An example

Present and discuss all the "standard" graphs for 3css.
This particular configuration was set up as an exercise to try to get very good separation at the crossings near the IP's, within about 56 half buckets of either B0 or D0.

This is not an optimized solution.
Mention sep settings
Rather than use the horizontal separators at B17, this assumes we have 2 modules at B48. In this lattice with 35 cm beta*, the horz phase advance between the B11 and the B17 horizontal separators is about 2*pi*(.90). They are nearly degenerate and often end up at high voltage and fighting each other. The B48 location is at a much better phase location, about 2*pi*(3.32) in horz phase from the separators at B11.
Rather than use the horizontal separators at F17, this assumes we have 2 modules at D48. This is because with both the RF system and the injection point at F0, space around F0 will be extremely tight, whereas space near E0 will be freed up.
Give table of sep. settings ?
HB48 is at -188 kV. If the C0 abort is ripped out, there may be room for more separators modules near here.
VA17 is at 217.6 kV. There is room at VA17 for more separator modules if the Schottky pick ups are moved.
VA49 is at -112 kV. This is close to what it can do.
Separator settings are not presently realistic, but we could probably find ways to achieve this basic configuration. Again though, keep in mind that this is not intended to be a real solution. Its only an exercise.
diag sigma sep
short vert helix +- 8.5 sigma
short horz helix +-10 sigma
long vert helix +-12 sigma
long horz helix +-6.5 sigma
Short vert helix and Long horz helix are somewhat smaller than we would like. Again these values are primarily intended to give good separation near the IP's. One of the questions is whether this is sufficient separation in the arcs.
xix, xiy, xisq cos, xisq sin vs arc
In the long helix, the vert sigma separation is larger than the horz separation.
So the points with the smallest sigma separation are where the separation is mainly horz and the vert separation is near zero. This corresponds to positive vertical tune shifts.
The largest peaks have the vertical sigma separations closest to zero at locations of peak vert. beta
Similarly in the short helix, positive horz tune shift peaks occur at analogous places. Negative horz tune shift peaks occur where the diag sigma sep is the smallest.
Note the opposite signs of the bbsq cos components near the 2 IP's.
These contributions will largely cancel.
Through the arcs, the horizontal and vertical betatron phases advance together and very nearly 2pi*(0.25) apart. Consequently the bb coupling component mainly appears as the sin like component. Only near the 0 locations are the horz and vert phases nearly in phase.
Usual comments that we are mainly concerned with the global coupling components.
We really have not looked at the (phix + phiy) components.
One point apiece with large xix and xiy near D0. B0 looks much better.
We can essentially switch these and make the two points with large xix and xiy appear near B0, with D0 looking much better.

But can't make both B0 and D0 look as good as B0 because of links between signs of kicks needed, e.g. at B11 and C49. Also because of overall sign requirement on crossing angles at B0, D0 to make coupling cancel.

Show a separate graph for bunch by bunch xiy vs xix for zero amp particles for say sigs of 37.1 cm.

Show the version with the points labeled with the bunch no.s The "upper tier" of points are the points within 2 of the ends of the trains or subtrains.

Comment that a different bunch length displaces this graph (give values) but does not change the pattern or contribute to the differences between the tune shifts for the different bunches (at least not the way that we are handling it.)

Show for all crossings and show another version with arc contribution only ?

Point here is that arcs have a significant contribution to the spread in the tune shifts between the different bunches. As far as the tune shifts for zero amp. particles are concerned, we need more separation in the arcs. Probably particularly for the short vert and the long horz pieces of the helices, which, as mentioned previously, are a little smaller than we would like.

xisq sin vs xisq cos for zero amp part

usual caveats -- we've chosen to compute coupling and tune shifts separately, actual tunes will be determined by both...

Although 5 points (1 above, 4 below) are separated from the main cluster, the coupling does not show the separation of the bunches within 2 of the ends of the trains or subtrains seen in the tune shifts.

range in coupling is probably acceptable.

If exactly decouple bunches in the middle, range of global tune splits will be sqrt((.0110/2)^2 + (.0055/2)^2) = .006

bunch by bunch positions and angles ?

Ranges look pretty reasonable.

Describe and give equations for tune shifts vs. amplitudes

No energy offsets.

Would be nice to at least take a quick look at the effects of an arrival time offset on the tune shifts from the main IP's.

Define amplitude.

specifically mention the bugs in the calculations in the snowmass paper

bunch length factor of 2 too large

amplitudes factor of sqrt(2) too large. -- could refer to this as not clearly defining what was meant by amplitude. But because of the population of particles for the histogram, snowmass is wrong.

Show min, max, range plots of tune shift vs arc

Not surprising points with the largest ranges tend to be points with large tune shifts for zero amp particles. But for points in arc, range (0 to 4 sigma) is less than size of zero amp tune shift.

Surprising to us that there is so little range in the xix in the long helix or in the xiy in the short helix.

A better way to view this is probably that the small separation in the other plane makes the range of xix greater in the short helix and the range of xiy greater in the long helix.

Now start looking at all 3 configurations again
We are going to work up to showing graphs of the distributions of particles in the tune plane for all the pbar bunches. While these graphs are important in themselves, they are more meaningful if we know how the different crossing points contribute, particularly in that we are still trying to use these calculations to understand and to design better separation schemes. Also because the tune footprint is not the only parameter of importance. As important is how strongly the beam beam interactions at the different crossing points drive different resonances. These resonance driving terms can be calculated (although we have not yet begun that), But we can start to get a very qualitative feel for the strengths of some of these resonances from the size of the tune spreads. That is a small spread in tune shifts with amplitude *suggests* that certain resonances will be weak.

Show 3 A17 footprints from crossings >28 half buckets from the IP's, No contours shown because they couldn't be seen since footprints are so small.

A17 is a "typical" bunch. With the exception of the bunches within 2 of the ends of the trains or sub-trains, the variation of the tune shifts with amplitude of the other bunches look very similar to A17. There are differences in the zero amp. tune shifts.

Main point here is that, despite the few small spikes seen in the range of the tune shifts in the arcs, the tune spread from arcs is very small. (Small in relation to the contributions to the tune spreads

for this bunch from other regions, which we will show shortly.) As far as tune spreads are concerned we've got enough separation in the arcs.

While all 3 cases are small, the 100 urad case has a larger xiy spread than the others.
100 urad case has poor diag sigma sep at several points in the short helix.
Problem is that after the "middle" separators in the short helix, the horz and vert separations are too close in phase, rather than being pi/2 out of phase. For the zero amp.
particles, this means that the effect of this point is mainly in the coupling and not in the tune shifts.
Four points in the short helix with diag sigma sep less than 5. These points have diagonal sigma separations of 3.3, 3.9, 4.5, and 4.9. By itself, the point with 3.3 contributes xix and xiy spread of about .0014, not terribly large, but noticibly larger than the other points in the arcs. This particular point is not a point where A17 sees a proton bunch, so the effect of this particular point is not shown in the figure.
We believe that this problem is not intrinsic to all 100 urad configurations, but rather is a characteristic of this particular case.

Show 3 A17 footprints from all crossings except main IP, show contours
(This will most clearly show differences in crossing angles.)

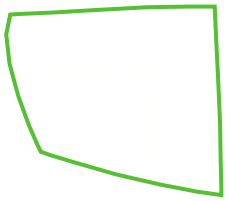

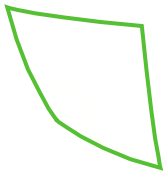

Describe contours. NOT contours of equal population. The heavy, black contour connects the (0,0), (0,2), (2,0), (2,2) points.
(Mention that contours were not shown in the >28 half buckets figure because the tune spread was so small that the contours would not be seen clearly.)

For all cases, a particle with zero amp. is at the bottom left corner.
For zero horz amp, as the vert amplitude increases, the points move up the left side.
For zero vert amp, as the horz amplitude increases, the points move along the bottom. Particles with the largest amplitudes shown in both planes (4,4) are at the top right.

Make a table of estimated areas enclosed by 2, 3, and 4 contours. ??
For a gaussian distribution,
About 3/4 have both horz and vert amps less than 2 sigma
95% of the particles have both horz and vert amps less than 2.72 sigma
97.8% have both the horz and the vert amp less than 3 sigma.

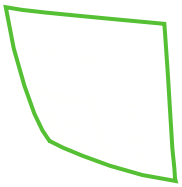

The nnpp2.136ppnp case has min diag sigma sep of 3.3 and 3 points with dss < 4, compared to pnpp3css.136nppp which has min dss of 3.5 and only 2 points with dss < 4. The point of showing the nnpp2.136 plot is that 0.2 diff in min diag sigma sep does make some difference in the footprint, especially on the 2 contour.
3css No B0, D0 3c contour has an area of about (.0072)^2 = 52.e-6
nnpp2 No B0, D0 3c contour has an area of about (.0087)^2 = 75.e-6

Also start to get some idea of sep neccessary.
For 170 urad case, where min diag sig sep is about 4.4, start to see points spreading out between 2.5 and 3 sigma. (4.4 - 2.7 = 1.7)
For 136 urad case, where min diag sig sep is about 3.3 or 3.5, start to see points spreading out between about 1.5 and 2 sigma. (3.4 - 1.7 = 1.7)
For 100 urad case, where min diag sig sep is about 2.4, start to see points spreading out almost immediately, between about 0.5 and 1 sigma. (2.4 - 0.7 = 1.7)

Consider 100 urad case. A particle with an amplitude of zhat, spends
about 40% of the time at displacements of 0.8(zhat) or greater, and
about 50% of the time at displacements of 0.7(zhat) or greater.
z beam beam kicks peak near z of about 1.5 sigmaz, displ in other plane < about 1 sigma

Strong points are within +-2 of the IP's.
At the +-1 points, both the horz and vert sig sep are about 3/sqrt(2) = 2.1
At the +-2 points, one is still about 2.1, the other is about 3.3

At particle amps of between 0.5 and 1 sigma, particles are getting within about 1 to 2 sigma (in both planes) from the opposing beam's core and are starting to see the strong beam beam kicks associated with the core of the opposing beam.

At particle amps of about 3.5 sigma, particles are getting to the edge of the strong beam beam kicks on the far side of the opposing beam's core. This is about as strong an effect as it gets from these *first few* near misses. The effect from these first few near misses will stay about the same, fall off slowly as the amplitudes continue to increase.
Little change between 3 and 6 sigma.
Around 7 sigma arc crossings are starting to be important.
But as amplitudes increase further, they are getting out to arc separations. At other crossing points, they will be starting to get near the core of the opposing beam.

Show the 6 (3angles X 2 bunch lengths) main IP only footprints

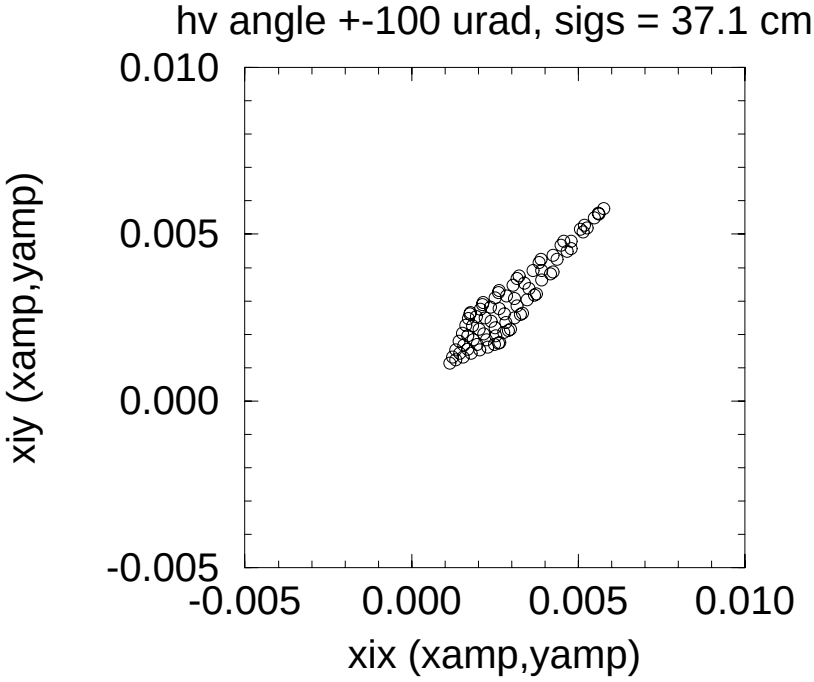
hv angle +-100 urad, sigs = 37.1 cm
0.010
0.005
0.000
-0.005
xiy (xamp,yamp)
-0.005
0.000
0.005
0.010
xix (xamp,yamp)

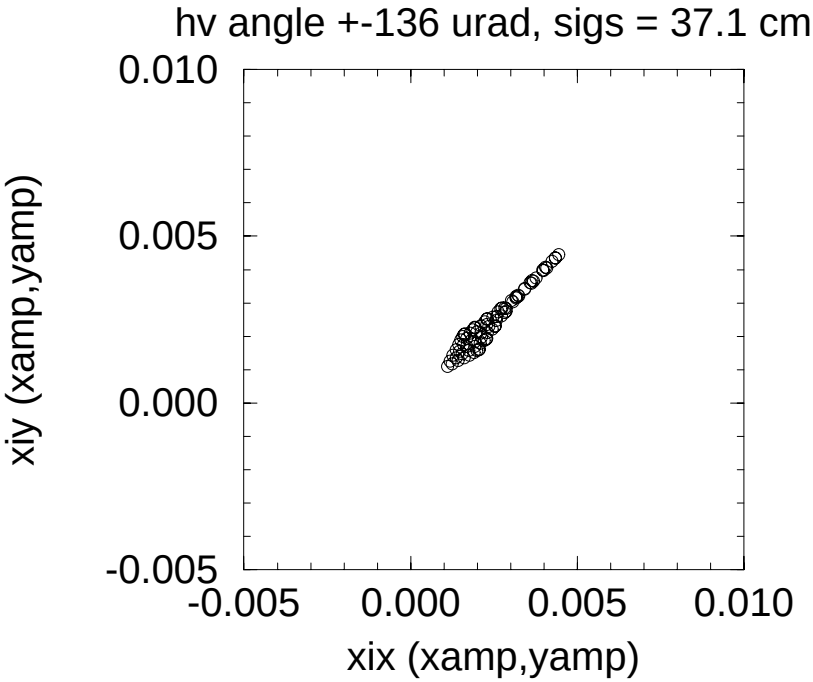
hv angle +-136 urad, sigs = 37.1 cm
0.010
0.005
0.000
-0.005
xiy (xamp,yamp)
-0.005
0.000
0.005
0.010
xix (xamp,yamp)

For 170 urad, sigs = 37.1 cm, upper half of the footprint is twisted.
Tune shifts for small amp particles decreases with increasing crossing angle and/or decreasing bunch length.
Emphasize that these have the mirror symmetry of the footprints for No B0, D0.
Small amplitude particles are in the upper right corner (for No B0, D0, these were in the lower left corner)

"Upper left" corner has (4,0) (For No B0, D0 this was on the bottom right corner.)
"Lower right" corner has (0,4) (For No B0, D0, this was on the upper left corner.)
"Lower left" corner has (4,4). (For No B0, D0, this was on the upper right.)
Because the points corresponding to a given amplitude are generally on opposite sides of the two footprints, when we add the effects, the resulting spreads are reduced.

Show the 6 A17, all crossings, footprints with contours

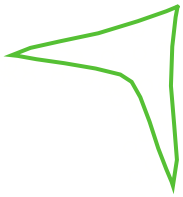

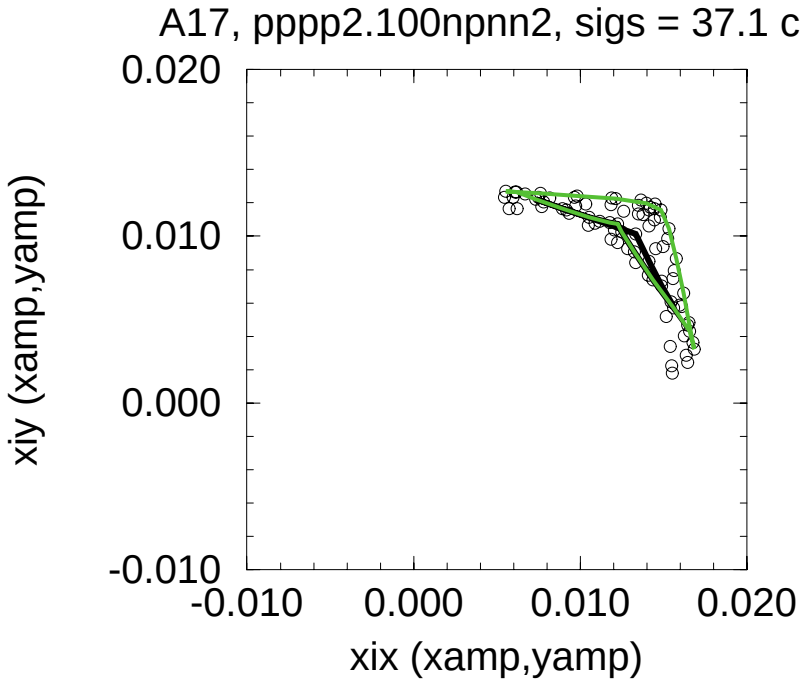
A17, pppp2.100npnn2, sigs = 37.1 cm
0.020
0.010
0.000
-0.010
xiy (xamp,yamp)
-0.010
0.000
0.010
0.020
xix (xamp,yamp)

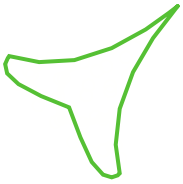

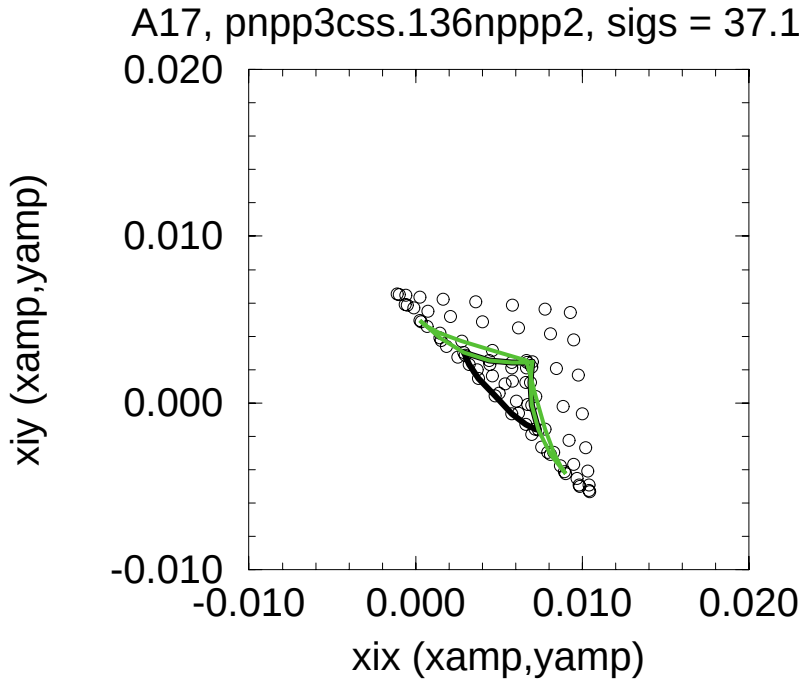
A17, pnpp3css.136nppp2, sigs = 37.1 cm
0.020
0.010
0.000
-0.010
xiy (xamp,yamp)
-0.010
0.000
0.010
0.020
xix (xamp,yamp)

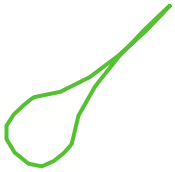

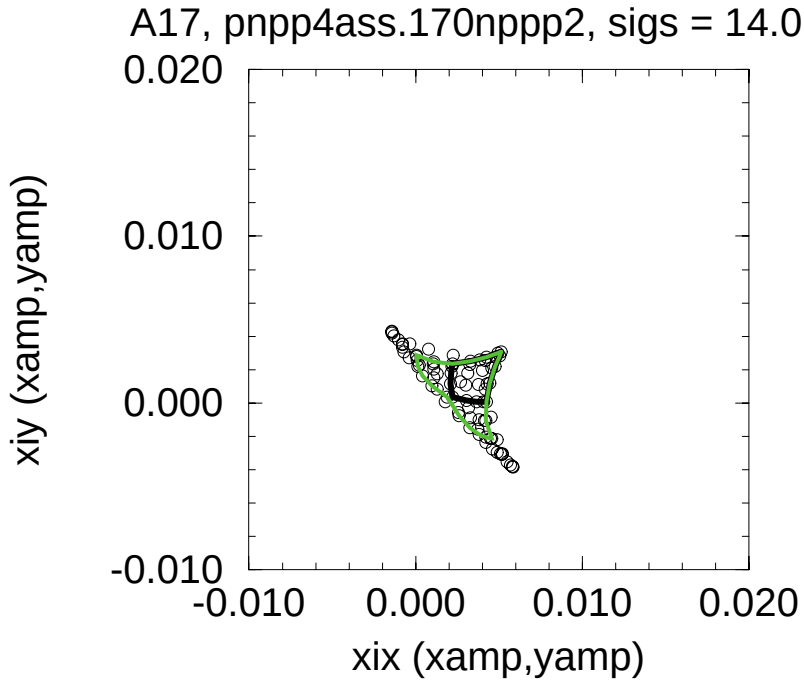

These are just the "sum" of the figures for the main IP only and the No B0, D0 footprints.
The No B0, D0 footprints are generally wider in the (xiy - xix) direction
and the Main IP footprints are quite narrow in the (xiy - xix) direction.
The Main IP footprints are generally wider in the (xiy + xix) direction.
Roughly speaking, adding the Main IP tune shifts to the No B0, D0 tune shifts turns the

No B0, D0 footprint "inside out" along the (xix + xiy) direction.
For the sigs=37.1 cm cases, the tune shifts from the Main IP's and the No B0, D0 along the (xix + xiy) direction happen to be similar in size and opposite in direction. The resulting cancellation produces a footprint occupying less area in the tune plane than the No B0, D0 footprints.
In particular for the 100 urad case with sigs = 37.1 cm, the tune shifts from the Main IP's and the No B0, D0 along the (xix + xiy) very nearly cancel. The resulting footprint appears flattened and occupies a relatively small area in the tune plane. We did not design the 100 urad case to have this behavior, this just happened to work out this way.

For the sigs = 14.0 cm cases, there is still some cancellation, but the larger Main IP tune shifts tend to dominate the other crossings.
For the 170 urad case with sigs = 14.0 cm, the tune shifts from the Main IP's and the No B0, D0 along the (xix - xiy) direction very nearly cancel. The resulting footprint has a needle appearance and occupies a relatively small area in the tune plane. Again this was not planned.

Show summary histograms for all 3 crossing angles and for both bunch lengths
Mention how the histograms were generated. 5000 particles per bunch, cut off at 4 sigma amplitudes, size of bins for hist. ...
Spread from zero amp tune shifts of different bunches is a significant contribution to area in the tune plane occupied. Zero amp tune shifts tend to spread more along the (xix - xiy) direction.
Can see from here that zero amp bunch spread goes down significantly for 170 urad case.
Most of the bunches have footprints very similar to A17. The bunches within 2 of the ends of the trains or subtrains have footprints with somewhat different shapes.

Show tune plane diagram and briefly discuss how well footprint fits.

Shape of the clear area is important.
Mention question of whether we can straddle the crossing resonance.
If we can, we have roughly twice as much space available and most of these distributions "fit".

Because we are close to the coupling resonance, more space along the direction (xix+xiy). For 135 urad, 100 urad, sigs = 37.1 cm, the distribution is more along the direction (xix-xiy). It would be easier to fit these between resonances if the tunes split the half integer, e.g.(.42, .59). (This is probably not a good idea. This point lies close to the more destructive nux + nuy resonance.We don't really have circuits set up to compensate this resonance.)

Continue to play with sep configurations
Work on modifying the lattice with an eye towards improving these beam beam tune spreads.
Working on several schemes to reduce the number of bunches within 2 of the ends of the bunch trains or sub-trains.
1) Fast inj. kicker with rise time of about 132 nsec
2) Shiltsev's fast inj kicker

3) Forming an entire bunch train in the Main Injector at inj.
   8 gev lifetime questions
   Multi batch coalescing -- Concerns with beam loading.
4) Get rid of one or more of the abort gaps
These schemes will cluster *most* of the bunches more tightly, but there will still be a few on the outskirts.

In an era when we are recycling the pbars at the end of a store and where the experiments request that we hold down the peak luminosity to keep the number of interactions per crossing down, the loss in luminosity from a large crossing angle may not hurt the integrated luminosity too much.

We believe we are making good progress on the spread in the tune shifts of the zero amp. particles in the different bunches and on the spread in tune shifts vs. amplitude.

Once we have solutions (lattices and separator configurations) we are satisfied with for these considerations, we intend to continue on to calculations of resonance strengths for nearby resonances, some particle tracking, etc...

4.9 Luminosity Leveling

The peak luminosity of 10^{33} $cm^{-2}sec^{-1}$ with 100 bunches per beam results in about 10 interactions per bunch crossing. It is difficult (and expensive) to build high performance detectors to operate in this environment. One possible operational scenario involves a technique known as "luminosity leveling". The idea is that the luminosity is held at a maximum value–say 0.5×10^{33} $cm^{-2}sec^{-1}$–during the initial part of the store and kept constant for as long as possible. The luminosity modulation could be accomplished, in principle, by varying any of the beam parameters on which the luminosity depends such as crossing-angle, bunch length, β^*, beam separation, etc. A simulation of luminosity leveling is shown in Figure 37 for the nominal parameters in Table II. The loss of luminosity from intrabeam scattering and residual gas effects is the same for both stores, but the luminosity limited store retains more antiprotons (fewer collisions) and has a higher luminosity at long times in the store.

The limited store yields 23.4 pb^{-1} in 14.0 hours (a 13 hour store plus one hour for shot setup) for an average luminosity of 1.67 pb^{-1}/hr compared to 36.2 pb^{-1} in 15.6 hr and an average luminosity of 2.32 pb^{-1}/hr for the unlimited store. The average luminosity obtained with a luminosity leveled store is less sensitive to the initial antiproton bunch intensity than a unleveled store, but the highest integrated luminosity is obtained in either case with the highest possible initial antiproton intensity. The loss of luminosity from leveling depends on the store parameters: the importance of the antiproton intensity to the lifetime, the amount of luminosity reduction desired, and the length of the store.

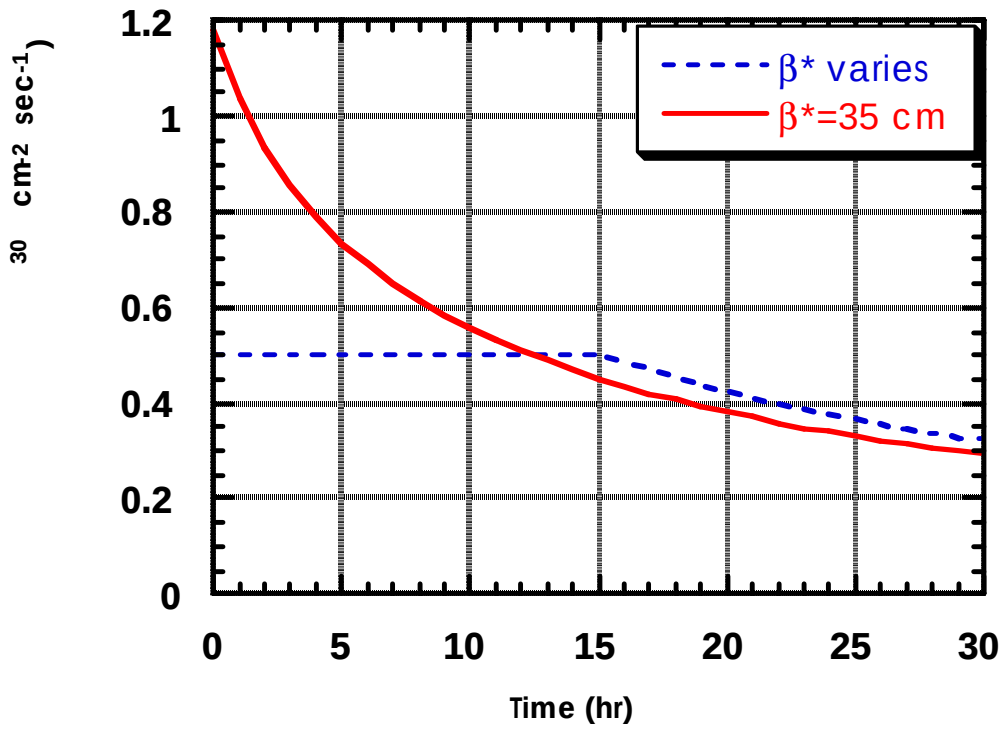

Figure 37. A store with the nominal parameters and $N_{\bar{p}} = 27 \times 10^{10}$ is compared to an otherwise identical store where β^* is varied to maintain a constant luminosity of 0.5×10^{33} $cm^{-2}sec^{-1}$ for as long as possible keeping $\beta^* > 35$ cm.

It should not be supposed that luminosity leveling is trivial or even straightforward. An enormous amount of effort is invested in minimizing beam loss by adjusting orbits, tunes, and chromaticity when the beams collide. The techniques that are used to modulate the luminosity may have adverse effects on the loss rate. One leading candidate to implement luminosity leveling is to modulate the beta function at the interaction point. Our experience is that changes to magnet excitation are likely to result in increased loss rates. It is not clear how well we will be able to control the beam loss rates when changes are made to the machine parameters to keep the luminosity constant.

5. Summary of upgrades required

The following tables are intended to provide a convenient summary of the major technical efforts necessary to implement the TeV33 scenario as outlined above. Table XVII summarizes the R&D efforts required. All of these R&D projects represent an extrapolation of

existing techniques; they are not design efforts utilizing proven technology. If the R&D should prove to be unsuccessful an alternative technology would have to be identified. Possible alternatives are discussed in section 6.

Table XVII. Summary of R&D projects required for Run III

R&D Project	Status
Electron Cooling	underway
4-8 GHz Pickup Design	underway
4-8 GHz Signal Transmission	underway
8-16 GHz cooling technology	deferred
Superconducting rf	deferred
Tevatron Kicker Bump Magnet	underway
Liquid high gradient lithium lens	deferred
Slip stacking	underway
Pbar aperture definition	underway

Table XVIII. Summary of upgrades required for Run II and Run III

Construction Project	Time Scale
Kicker Bump Magnet	Run II
Debuncher Cooling Improvements**	Run II
Accumulator Lattice Change*	Run II
Pbar Target Sweeping *	Run II
2-4 GHz Accumulator stack tail upgrade*	Run II
Tevatron Short Batch Kicker*	Run II
AP-5 beam line	Run II^{+}
Lithium lens (to 900 T/m)	Run II^{+}
Main Injector gammat-jump	Run II^{+}
Main Injector Coalescing rf	Run II^{+}
Improved low level agility (Slip stacking)	Run II^{+}
Beam loading compensation (Slip stacking)	Run II^{+}
Pbar aperture upgrade	Run II^{+}
Fiber optic links for 4-8 GHz	Run II
4-8 GHz Debuncher transverse cooling	Run III
4-8 GHz Debuncher longitudinal cooling	Run III
4-8 GHz Accumulator stack tail upgrade	Run III
Electron cooling	Run II^{+}
Superconducting RF	Run III

+These upgrades could possibly be implemented at the beginning of Run II or sometime during Run II. However, they are not required to achieve the Run II performance goals and they are not part of the standard plan.

**The Debuncher Cooling Improvements will use 4-8 GHz technology if the on-going R&D is successful in time to be implemented for Run II. Even if this effort is successful, further upgrades will be necessary for Run III; these are listed as the "4-8 GHz Debuncher" cooling upgrades.

6. Risks & Alternative approaches

6.1 Risks

The TeV33 plan that has been outlined has some obvious risks in that it relies on technology that is still being developed. The most difficult technologies are also the most critical, namely,

1) High sensitivity stochastic cooling pickups and kickers for the 4-8 GHz band.
2) Electron cooling of 8 GeV antiprotons.

The plan to increase the antiproton acceptance to 32π mm-mrad is clearly feasible with an unlimited budget. However, we have not yet determined what modifications are required to reach this goal.

Slip stacking has not been demonstrated at Fermilab, but has been studied at CERN. Other bunch coalescing techniques are in routine use at both CERN and Fermilab. We expect a more difficult time - at least with the scenario outlined in this report - because of beam loading and other collective effects.

The Tevatron has never operated with a non-zero crossing-angle. The size of crossing angle effects depends on the scaled angle:

$$\alpha' = \frac{\alpha \sigma_z}{\sigma_t} \qquad [18]$$

The problem of synchro-betatron resonances was first appreciated when the DORIS storage ring attempted to run[33] with α'=0.45. The LHC is proposed to operate with α'=0.5 and a total beam-beam tune spread of 0.015, while the TeV33 parameters are a more aggressive α'=1.8 with a total tune spread of about 0.025. More detailed calculations are useful, but the operational limits of the Tevatron collider with a crossing angle will not be definitively known until experiments are performed in Run II.

6.2 Alternatives

It appears that there is no alternative to the requirement for higher antiproton production rates and higher cooling rates. The development of 4-8 GHz cooling technology also seems essential. The only known alternative–more cooling steps or parallel paths–seems impractical to implement at a reasonable cost. It might be possible to upgrade the Run II Recycler stochastic cooling system as an alternative to the electron cooling system proposed for TeV33. While an optimized 4-8 GHz stochastic cooling system should, in principle, be adequate to accumulate the required antiproton flux, it would have a much slower cooling rate and provide larger final emittances than even a modest electron cooling system.

A wide variety of schemes for increasing the antiproton flux are possible. Any scheme (like slip stacking) that raises the proton intensity could be used. Alternatives include an increased Linac energy (say to 800 MeV), a new or rebuilt Booster, betatron stacking and possible variations on the slip stacking scheme proposed for TeV33. One particular proposal that has been developed in some detail involves targeting the full Main Injector circumference.[34] This scheme is attractive because it does not require any improvements in the Main Injector intensity nor in the injector chain. However, it does require technological advances in kicker technology and, perhaps more importantly, has an impact on the NUMI project, which plans to use 5/6 of the Main Injector protons for neutrino production.

The bunch loading scheme, crossing angle, and optics in the Tevatron have a number of options that have not been explored in much detail. In particular, it seems likely that we will want to minimize bunch-by-bunch tune shifts by adopting a more uniform loading scheme than the one displayed in Figure 29. One specific proposal to build a fast strip-line kicker with a 20 nsec rise-time is being considered. More ambitious projects aimed at compensating some or all of the beam-beam interaction have been discussed, but nothing has emerged as a serious candidate for consideration.

7. Conclusion

An upgrade in the luminosity of the Tevatron proton-antiproton collider to the vicinity of $L=10^{33}$ cm^{-2}sec^{-1} appears to be feasible provided that the technological advances described in this report can be realized. A necessary, but not sufficient, condition for the increase in luminosity is a substantial increase in the antiproton accumulation rate. We have proposed a plan to increase the stacking rate by a factor of 4. Another necessary condition is a large increase in the number of bunches colliding in the Tevatron. Our ability to avoid adverse effects from the beam-beam interaction is a primary concern, and an area that is actively being studied. However, based on the beam-beam footprints that have been obtained, colliding large numbers of bunches appears to be feasible.

References

[1] TheTeV2000 committee report (unpublished), but currently available on the World Wide Web site http://www-theory.fnal.gov/tev33.ps.
[2]Fermi National Accelerator Laboratory, “The Fermilab Main Injector Technical Design Handbook,” unpublished, but available on the world-wide-web at http://www-fermi3.fnal.gov/maininjector/main_injector.html.
[3] G. Jackson, “The Fermilab Recycler Ring Technical Design Report,”, Fermilab Report No. TM-1991 (1996), unpublished.
[4] D. Herrup and D. McGinnis, private communication. There is a better reference, I think.
[5] D. Boussard and Y. Mizumachi, "Production of Beams with High Line-Density by Azimuthal Combination of Bunches in a Synchrotron", CERN-SPS/ARF/79-11; 1979 IEEE Particle Accelerator Conference (1979).
C. Ankenbrandt, "Slip-Stacking: A New Method of Momentum Stacking" Fermilab FN-352 (1981).
[6] N.V. Mokhov, "The MARS Code System User's Guide, Version 13(95)", Fermilab Internal Note No. FN-628 (1995), unpublished. The older MARS10 program is described in Fermilab Internal Note No. FN-509 by the same author.
[7] CM Bhat and NV Mokhov, *"Calculation of Beam Sweeping Effect for the Fermilab Antiproton Source"*, Fermilab-TM-1585 (1989)

[8] FM Bieniosek, K Anderson and K Fullett, *"Requirements for a Beam Sweeping System for the Fermilab Antiproton Source Target"*, Proc. of the 1995 US Particle Accelerator Conference, p1939. Dallas (1995); and FM Bieniosek, *"A Beam Sweeping System for the Fermilab Antiproton Production Target"*, Fermilab-TM-1857 (1993)
[9] G. Dugan et al., IEEE Trans. Nucl. Sci. **30**:3660-3662(1983)
[10] S.O'Day and K.Anderson, Proc. 1995 US Particle Accelerator Conference, Dallas, Texas
[11] Gregory I. Silvestrov, "Lithium Lenses for Muon Colliders," AIP Conference Proceedings 372, p. 168, 1995 (Beam Dynamics & Technology Issues for mu+mu- Colliders).
[12] P.P. Bagley, et al., Summary of the TeV33 Working Group, Snowmass 1996 Proceedings.
[13] G. Dugan, "Shielding Scaling Calculations,", Fermilab Note No. TM-1714 (1991), unpublished.
[14] J.D. Cossairt, Fermilab unpublished ES&H note No. EP Note 8.
[15] S O'Day, FM Bieniosek, *"8.9 Gev Pbar Yield Measurements at the Fermilab Antiproton Source"*, Nuclear Instruments and Methods ,A343, p343 (1994)
[16] S O'Day, FM Bieniosek, *"Pbar Production Measurements at the Fermilab Antiproton Source"*, EPAC 94 Proceedings, p2438, London (1994)
[17] Fermilab III Accelerator Upgrade Phase 1 (1990/94), unpublished.
[18] D Olivieri, "A Dynamic Momentum Compaction Factor Lattice for Improvements to Stochastic Cooling in Storage Rings", Dissertation thesis for the University of Massachusetts, Amherst (1996)
[19] Fermi National Accelerator Laboratory, "Design Report Tevatron I Project," (September 1984), unpublished.
[20] S. van der Meer, "Stochastic Stacking in the Antiproton Accumulator," CERN Report No. CERN/PS/AA/78-22 (1978), unpublished.
[21] MEB E-Cool Design Report 1992, Indiana University Cyclotron Facility (October 1992)
[22] National Electrostatics Corporation Newsletter, Fall 1990 (NEC, Graber Rd., Box 620310, Middleton, WI 53562 USA.
[23] J.A. Ferry, et al., "Accelerator terminal voltage stability", NIM B64 (1992) 309-312.
[24] T. Ellison, R. Brown, and B. DeVries, "The IUCF electron cooling system collector performance", NIM B40/41 (1989) 864-869.
[25] S. Nagaitsev, et al., " The development of the technology for electron cooling in the 2-20 GeV/nucleon energy regime" in Proceedings of the 1993 Workshop on Beam Cooling, CERN Report No. 94-03, pp. 390-394.
[26] Ioanis Kourbanis, talk given to the TeV33 working group, :Proton bunch formation with variable spacing," May 13, 1996 (unpublished).
[27] P.P. Bagley, et al., "Summary of the TeV33 Working Group," Fermilab Note No. Conf-96-392 (1996), to appear in the Snowmass 1996 proceedings.
[28] Transverse head-tail instability
[29] Longitudinal head-tail instability
[30] 6x6 damper reference
[31] C. Crawford, Fermilab Report No. TM-1564, unpublished.
[32] S.D. Holmes, et al., "132 nsec Bunch Spacing in the Tevatron Proton-Antiproton Collider," Fermilab Report No. TM-1920 (1994), unpublished.
[33] A. Piwinski, "Limitation of the Luminosity by Satellite Resonances", DESY 77/18 (March 1977).
[34] W. Foster, "Multibatch P-bar Production via Snap Coalescing: A Plan to Produce Approximately 5x More Antiprotons/Cycle Using Mostly Existing Equipment," Fermilab Report No. TM-1902 (1994), unpublished.